Flight Reynolds Number Testing of the Orion Launch Abort Vehicle in the NASA Langley National Transonic Facility (Invited)

David T. Chan[*] and Gregory J. Brauckmann[†]

NASA Langley Research Center, Hampton, VA, 23681

A 6%-scale unpowered model of the Orion Launch Abort Vehicle (LAV) ALAS-11-rev3c configuration was tested in the NASA Langley National Transonic Facility to obtain static aerodynamic data at flight Reynolds numbers. Subsonic and transonic data were obtained for Mach numbers between 0.3 and 0.95 for angles of attack from -4 to +22 degrees and angles of sideslip from -10 to +10 degrees. Data were also obtained at various intermediate Reynolds numbers between 2.5 million and 45 million depending on Mach number in order to examine the effects of Reynolds number on the vehicle. Force and moment data were obtained using a 6-component strain gauge balance that operated both at warm temperatures (+120 °F) and cryogenic temperatures (-250 °F). Surface pressure data were obtained with electronically scanned pressure units housed in heated enclosures designed to survive cryogenic temperatures. Data obtained during the 3-week test entry were used to support development of the LAV aerodynamic database and to support computational fluid dynamics code validation. Furthermore, one of the outcomes of the test was the reduction of database uncertainty on axial force coefficient for the static unpowered LAV. This was accomplished as a result of good data repeatability throughout the test and because of decreased uncertainty on scaling wind tunnel data to flight.

Nomenclature

Symbols

A_{base}	Base area, ft^2
C_A	LAV axis axial force coefficient
C_l	LAV axis rolling moment coefficient
C_m	LAV axis pitching moment coefficient
C_N	LAV axis normal force coefficient
C_n	LAV axis yawing moment coefficient
C_p	Pressure coefficient
C_Y	LAV axis side force coefficient
D	CM heat shield diameter, in
d_2	Bias correction factor
L	Model length, in
P_t	Total pressure, psi
q	Dynamic pressure, psf
r	Radial location, in
r/D	Radial location normalized by CM heat shield diameter
Re_D	Reynolds Number based on crew module heat shield diameter, million
S_{ref}	Vehicle reference area, ft^2
T_t	Total temperature, °F
x	Axial location, in
x/L	Axial location normalized by model length
α	Angle of attack, deg
β	Angle of sideslip, deg
σ	Standard deviation

Units

°, deg	degrees
°F	degrees Fahrenheit
atm	atmospheres
ft^2	square feet
in-lbf	inch-pound force
lbf	pounds force
M	Million
MW	Megawatts

---

[*]Research Aerospace Engineer. Configuration Aerodynamics Branch. NASA Langley Research Center. Member AIAA.
[†]Research Engineer. Aerothermodynamics Branch. NASA Langley Research Center. Associate Fellow AIAA.

American Institute of Aeronautics and Astronautics

psf	pounds per square foot		FEA	Finite Element Analysis
psi	pounds per square inch		ISS	International Space Station
psia	pounds per square inch absolute		ITAR	International Traffic in Arms
psid	pounds per square inch			Regulations
	differential		JM	Jettison Motor
RPM	revolutions per minute		LAS	Launch Abort System
sec	seconds		LAT	Launch Abort Tower
			LAV	Launch Abort Vehicle
Acronyms			LEO	Low-Earth Orbit
3-D	3-dimensional		LN_2	Liquid Nitrogen
ACM	Attitude Control Motor		MRC	Moment Reference Center
ALAS	Alternate Launch Abort System		NASA	National Aeronautics and Space
AM	Abort Motor			Administration
AOA	Angle of Attack		NTF	National Transonic Facility
BMC	Balance Moment Center		OML	Outer Mold Line
BPC	Boost Protective Cover		OVERFLOW	OVERset grid FLOW solver
CAP	CEV Aerosciences Project		RTD	Resistance Temperature Detectors
CEV	Crew Exploration Vehicle		SBU	Sensitive But Unclassified
CFD	Computational Fluid Dynamics		TS	Test Section
CLV	Crew Launch Vehicle		UV	Ultraviolet
CM	Crew Module		V	Version
ESP	Electronically Scanned Pressure		WT	Wind Tunnel

I.   Introduction

THE Orion Crew Exploration Vehicle (CEV) was NASA's planned replacement for the Space Shuttle to carry future astronauts into orbit for missions to low-earth orbit (LEO) and the International Space Station (ISS) and for missions to the moon, to Mars, and beyond.[1] The CEV is similar in shape to the Apollo spacecraft, but significantly larger. The CEV was designed to launch atop the Ares I Crew Launch Vehicle (CLV), a two-stage booster employing both solid and liquid-fueled rocket motors. For crew safety, the CEV utilized a launch abort system (LAS) that is capable of pulling the Crew Module (CM) capsule away from the CLV in the event of an emergency on the launch pad or at any point along the ascent trajectory until nominal tower jettison. The combination of the LAS mated to the CM is referred to as the Launch Abort Vehicle (LAV).

The LAV, shown in Fig. 1, consists of an ogive-conical fairing that surrounds the CM and connects to a cylindrical tower containing three solid rocket motors used during an abort. The abort motor (AM) is a high-thrust, high-impulse engine utilizing four exposed, reverse-flow nozzles to quickly pull the CM away from the CLV. The attitude control motor (ACM) is used to provide steering and control of the vehicle during an abort and consists of a single solid rocket motor connected to eight axisymmetric nozzles arranged circumferentially around the tower and perpendicular to the centerline axis of the vehicle. The jettison motor (JM) lies approximately in the middle of the tower and is used to pull the launch abort tower (LAT) away from the CM in the final stages of an abort before the CM begins its free-flight. The JM employs four nozzles that are scarfed flush with the surface of the tower.

A typical abort sequence is shown in Fig. 2. In the event of an emergency, the AM fires to pull the LAV away from the CLV while the ACM fires to provide steering and control. After the AM burns out, the vehicle continues to coast, with the ACM providing trim near zero angle of attack. The ACM then turns the LAV to a heat-shield-forward orientation, damping out pitch rates prior to tower jettison. Pyrotechnic bolts discharge to separate the LAT from the CM, while the JM fires nearly simultaneously to clear the LAT from the CM prior to parachute deployment. The entire abort sequence takes approximately 20-30 seconds to complete.

Previous wind tunnel (WT) testing of the LAV have been conducted at Reynolds numbers that are about 10-30 times less than that of flight during an ascent abort. Computational fluid dynamics (CFD) has been used to predict a Reynolds number increment in order to scale the wind tunnel data to flight. However, there were no wind tunnel data at an intermediate Reynolds number or at flight Reynolds number in order to validate the CFD results. Therefore, the CEV Aerosciences Project (CAP) aerodynamic testing team set

out to obtain data at flight Reynolds numbers on the unpowered LAV in order to populate the aerodynamic database and also to validate and/or calibrate the CFD code predictions. The NASA Langley National Transonic Facility (NTF) was selected as the test facility because of its ability to obtain data at extremely high Reynolds numbers due to its total pressure capability ($\sim$8 atm) and through its use of liquid nitrogen to drastically decrease the temperature of the test gas (down to -250 °F).

The Orion LAV and its aerodynamics have been designated sensitive but unclassified (SBU) due to export control restrictions under the International Traffic in Arms Regulations (ITAR). Therefore, to comply with SBU rules, some details have been removed from plots and figures in this paper.

II. Experimental Program

This section provides details about the experimental program. A brief description of the experiment design, test facility, test model, instrumentation, and data reduction are given here.

II.A. Experiment Design

To determine the range of Reynolds number that the LAV would experience in flight, results from a flight trajectory simulation were used. The Reynolds number versus Mach number information was extracted for various ascent abort scenarios and data were collected from abort initiation to the start of the reorientation phase. Figure 3 shows that for the subsonic and transonic Mach numbers of interest, the LAV experiences a range of Reynolds numbers based on diameter between about 20 million to about 85 million (the crew module heat shield diameter is used as the reference length).

The NTF was chosen as the test facility to achieve the Reynolds numbers of interest, as no other U.S. facility can obtain these high Reynolds numbers. Figure 4 shows the operating envelope of the NTF in air mode at 120 °F and in nitrogen mode at -250 °F. The test conditions for the LAV are also shown for reference. One of the unique capabilities of the NTF is the ability to control Mach number, Reynolds number, and dynamic pressure independently. This is achieved through the independent control of Mach number, total pressure, and total temperature in the tunnel. This allows the isolation of Mach number, Reynolds number, and aeroelasticity effects[2,3] in a dataset. Figure 5 shows representative facility operating envelopes to illustrate this. However, the Mach number range of the NTF (Mach < 1.2) prevented testing in the high transonic to low supersonic range (1.2 $\leq$ Mach $\leq$ 1.6), which was of interest to the test team.

The suite of cryogenic-rated strain gauge balances that the NTF employs are typically sized for transport aircraft models, which experience large normal force and pitching moment loads. For a blunt-body vehicle such as the LAV, a larger axial force gauge is required. The standard NTF balances are oversized for the LAV in all components except for axial force, which is undersized. Since there were not enough resources (time and money) to fabricate a new cryogenic-rated balance sized specifically for the LAV, the decision was made to use one of the existing NTF balances. To allow for an increase in axial force capability, a finite element analysis (FEA) was performed on the balance with an overload on axial force, but with reduced loads on the other five components.

For model design, there were several factors to consider. The model needed to be large enough to accommodate the required internal instrumentation, but not so large as to increase tunnel blockage effects. It also needed to handle the loads generated at each of the test conditions without overloading the balance. It was decided that a 6%-scale model would suffice. At this scale, the blockage in the tunnel was about 1.1% and the model could also handle the loads generated at the high Reynolds number test conditions of interest.

The test matrix was designed with a few goals in mind. The matrix consisted of runs in air mode to obtain data at lower Reynolds numbers to match conditions of previous tests in different facilities and to obtain data at a Reynolds number that will allow some comparison between air mode and nitrogen mode. In nitrogen mode, the basic goal was to cover the predicted Reynolds number range from Fig. 3 by obtaining data at various intermediate Reynolds numbers and to reach as high a Reynolds number as possible at each Mach number within balance or facility capabilities. There were also sets of repeat runs in both air and nitrogen mode to be able to assess data repeatability. Figure 6 shows a summary of the pre-test goals for Mach number and Reynolds number coverage. For vehicle attitude, the test team wanted more positive angle of attack coverage, therefore, a 6° offset sting was chosen to allow a model angle of attack range of -4° to +22°. Angle of sideslip coverage spanned -10° to +10° through a combination of pitch and roll settings.

The main data products from the test were the 6-component static force and moment data from the

balance and the static pressure data from the electronically scanned pressure (ESP) units. In addition, the test section wall static pressures were used to provide a wall boundary correction to the balance data.

II.B. Facility Description

The National Transonic Facility (NTF) is a fan-driven, closed-circuit, continuous-flow, cryogenic, pressurized wind tunnel used to obtain aerodynamic data on sub-scaled vehicles at subsonic and transonic speeds up through full-scale Reynolds numbers for most flight vehicles.[4] The 8.2 feet x 8.2 feet test section is square but with corner fillets and is 25 feet long. The nominal test section configuration possesses six slots and seven re-entry flaps each in the top and bottom walls with a total bleed-through capacity of six percent to prevent the flow from choking the tunnel at near-sonic conditions.

The NTF can operate as a conventional pressurized wind tunnel using dry air as the test medium, where the free stream temperature is controlled by water-fed cooling coils located at the upstream end of the settling chamber. Additionally, the NTF can operate as a cryogenic pressurized wind tunnel using gaseous nitrogen as the test medium, where liquid nitrogen (LN_2) is injected and vaporized into the circuit flow using 296 nozzles in twelve injector bundles located just upstream of the fan to control free stream temperature. These two modes of operation (air and nitrogen) allow the tunnel to operate at temperatures between 120 °F and -250 °F and total pressures from 15 psia to 130 psia. Thermal insulation that resides inside the pressure shell minimizes energy consumption. Using this combination of pressure and temperature, the NTF has the ability to produce extremely high Reynolds number conditions. An overview of the NTF is provided in Fig. 7.

The tunnel drive system is powered by a variable speed motor that has variable maximum torque or power output. The compressor consists of a fixed pitch, single stage fan with variable inlet guide vanes. The drive system can be operated from 0 RPM to 600 RPM with a maximum power output of 100 MW, and the inlet guide vanes are varied to achieve the desired compression ratio to obtain fine Mach number control. This allows the NTF to achieve Mach numbers up to 1.2.

Model pitch angle is achieved by moving a large arc sector whose center of rotation lies in the middle of the test section. The arc sector can move nominally between -10.5° and +16.5°. Model roll angle is achieved through a roll drive located inside the strut support system. NTF does not possess a pure yaw mechanism; therefore to achieve angles of sideslip, the NTF uses a combination of model pitch and roll settings.

Multiple optical ports are located in the test section walls for use with cameras and lights for a variety of optical measurement techniques that include pressure and temperature-sensitive paints, target-tracking model deformation, and focused schlieren.

II.C. Model Description

The test article was a 0.06-scale (6%) model of the ALAS-11-rev3c configuration of the Orion LAV. At this scale, there was sufficient volume for instrumentation hardware, wires, and pneumatic pressure tubing. Outer mold line (OML) features greater than 0.5 inches full scale were represented in the model. Some noteworthy OML details include the ACM and JM nozzle cutouts as well as the AM nozzles. This model was an unpowered model, thus there were no jet plume simulations of the AM, ACM, or JM. There was also a system raceway underneath the tower and a cutout on the ogive for the system umbilical.

Since the model was subjected to adverse conditions in the NTF, such as extremely low temperatures and high dynamic pressures, it was made out of 13-8 PH H1150M stainless steel with a surface finish requirement of at most 16 microinches. The design consisted of a one-piece tower and one-piece ogive attaching to a finger-flanged joint on the balance adapter, where the angle of attack (AOA) package and ESP heated enclosures were also secured. The nose tip, raceway, and abort motor nozzles were installed onto the tower. The balance and sting exited the back of the model through the center of the heat shield, which was designed as two halves so that it could be installed last after all instrumentation was secured inside the ogive. In addition, cutouts were put into the heat shield halves to accommodate instrumentation wire bundle routing. The design minimized external fastener holes that would need to be filled, which was a concern for cryogenic model testing because of surface finish requirements. Figure 8 shows an exploded view of the model and a photo of the model in the NTF.

There were a total of 124 static pressure port orifices on the model arranged in rings at various longitudinal locations along the vehicle and at several radial locations on the CM heat shield. In almost all of the rings, the ports were placed at phi angles of 0°, 45°, 90°, 135°, 180°, and 270° with 0° defined as the top centerline

and increasing clockwise when looking upstream. There were a total of 26 ports on the tower, 36 ports on the cone, 36 ports on the ogive, and 26 port on the CM heat shield and bumper. Figure 9 shows the longitudinal and radial locations of the static pressure port orifices along the vehicle. The x/L value and the r/D value at each location are shown for reference.

Boundary layer transition strips consisting of cylindrical mylar tape dots were applied in longitudinal rows along the model at four radial positions and applied in circumferential rows at two longitudinal locations. The tape dots were 0.0066 inches in height and 0.05 inches in diameter, with a spacing of 0.10 inches between centers. Figure 10 shows the transition scheme used in the test. The trip height and location were determined using well-established trip sizing guidelines based on critical roughness height.[5,6] The longitudinal trip arrays were included in an effort to trip crossflow at higher angles of attack. The trip dots were only applied for runs in air mode (Re_D < 10 million). A set of runs also obtained in the air mode with no trip dots on the model to assess the effectiveness of the transition scheme. In nitrogen mode, the trip dots were not applied to the model because it was assumed that at the higher Reynolds numbers, the boundary layer would transition naturally, negating the need for trip dots.

The model was supported in the test section using a combination of the NTF 6° offset stub sting and a straight sting. Figure 11(a) shows a sketch of the assembly in the test section. The location of the center of rotation of the arc sector and the end of the test section are shown for reference. The arc sector can move nominally between -10.5° and +16.5° and the 6° offset stub sting was chosen in order to achieve more positive angles of attack for the model, effectively giving a range between -4.5° and +22.5° angle of attack. Since the model resided close to the center of rotation of the arc sector, it remained pretty close to the centerline of the test section as it moved to an angle of attack. Figure 11(b) shows the location of the model in the test section at -4.5°, +6°, and +22.5°.

II.D. Model Instrumentation

The NTF-118A balance was used to acquire force and moment data on the model. It is a NASA Langley-designed 6-component strain-gauge balance fabricated from Aermet 100, an ultra-high strength alloy steel. It has exceptional hardness, tensile strength, fracture toughness, and ductility properties and can be used at both warm and cryogenic temperatures. It is a nominally 2-inch diameter balance and the metric end attaches to the model balance adapter with a 0.625-inch diameter dowel pin. On the non-metric end, it attaches to the sting through a tapered joint secured with set screws. The balance had 9 resistance temperature detectors (RTD) at various locations to monitor balance temperatures and temperature gradients. Figure 12 shows an outline drawing of the balance.

Table 1 shows the design loads for the balance as well as the maximum aerodynamic loads that were expected during the test. The expected axial force load is shown in red to highlight the overload as compared to the balance design load. The maximum expected loads and, in particular the overload in axial force, were shown by a FEA to have the required factor of safety. The full-scale calibration accuracies of the balance are also shown for reference.

Table 1. Balance load ranges for NTF-118A balance.

Component	Calibrated Load	Max Test Load Expected	Calibration Accuracy (2σ)
Axial Force	700 lbf	1,200 lbf	±1.61 lbf
Normal Force	6,520 lbf	1,800 lbf	±3.91 lbf
Side Force	4,000 lbf	800 lbf	±6.40 lbf
Rolling Moment	8,150 in-lbf	300 in-lbf	±12.23 in-lbf
Pitching Moment	12,800 in-lbf	6,800 in-lbf	±14.08 in-lbf
Yawing Moment	6,400 in-lbf	2,400 in-lbf	±17.92 in-lbf

Model angle of attack was measured with an onboard accelerometer package with a NTF 204 series designation. This cylindrical package houses two Q-Flex servo accelerometers to measure model angle-of-attack and four dynamic accelerometers to measure a dynamic phenomenon known as sting whip. The package also contains internal heater elements to keep the accelerometers thermally conditioned while at cryogenic test conditions. Figure 13 shows a drawing of the AOA package and its location inside the model.

American Institute of Aeronautics and Astronautics

A second AOA package located in the arc-sector acted as the primary measurement package during runs at non-zero sideslip angles.

Static pressure measurements were acquired with two 15-psid ESP modules located inside the model. The modules were mounted inside insulated heated enclosures (Fig. 14) in order to survive the cryogenic test temperatures. The enclosures were made from hard insulation foam and were lined on the inside with a copper plate heated by flexible polyimide element heaters. Flexible tubing was required to connect the 0.040-inch (outer diameter) stainless steel tubing of the model to the ports on the ESP modules.

II.E. Test Execution

The test was run at temperatures of +120 °F and -250 °F at Mach numbers from 0.3 to 0.95 for Reynolds numbers between 2.5 million and 45 million based on CM heat shield diameter. Mach numbers above 0.95 could not be achieved due to blockage. Angles of attack between -4° and 22° and angles of sideslip between -10° and 10° were achieved.

Most of the planned test matrix runs were acquired, however there were some Mach and Reynolds number combinations that could not be reached (Fig. 15). This was mainly due to model and support system dynamics. NTF historically experiences yaw dynamics[7] caused by the arc sector, which feeds upstream to the model because the model is mounted on the end of a long cantilevered sting. Because the vehicle does not have any significant rolling moment generators, the expected aerodynamic rolling moment was only around 300 in-lbs, however, during the test, dynamic rolling moment loads of over 1000 in-lbs were measured. Spectral analysis of high frequency dynamic data showed that the rolling moment dynamics were caused by the dominant yaw dynamics. A couple of pins in the model were under-designed to handle the increased rolling moment load, and therefore, some of the highest Reynolds number conditions could not be tested.

Also, due to time and LN$_2$ resource constraints, all planned sideslip angles were not obtained at each Mach and Reynolds number combination tested. The only Reynolds numbers that had full sideslip angle coverage at every Mach number were 4.5 and 20 million. Figure 16 shows a summary of the sideslip angle coverage for the test. It can be seen that 0° and 10° sideslip angles were the most common.

II.F. Data Reduction

The reference axes and definitions of various quantities for the LAV are given in Fig. 17. All aerodynamic force and moment data are presented on the LAV aerodynamic axis as shown in Fig. 17(b). This coordinate system was chosen to take advantage of symmetry characteristics on the vehicle and is rotated 13.3° from the body axis.[8] The moment reference center (MRC) for the LAV is located at the theoretical apex of the crew module.

The balance data, referenced at the balance moment center (BMC), are reduced to engineering units according to the standard facility data reduction process[9] and then transferred to the model moment reference center (MRC). A correction to axial force due to the presence of the cavity in the heat shield was also applied. The average static pressure inside the cavity was corrected to the average static pressure on the heat shield using the inner ring at r/D = 0.231, and coupled with the cross sectional area of the cavity, provided the correction to the model axial force. The magnitude of this correction was small when compared to the total axial force. Finally, the data was converted to coefficient form using freestream dynamic pressure and appropriate reference areas and lengths. Some of the coefficients were adjusted for model buoyancy corrections and tunnel wall corrections.[10, 11] The freestream flow conditions were determined by the standard facility flow conditions subroutines, which are based on real-gas equations and account for the slight differences in properties between air and nitrogen.

During zero angle of sideslip runs, model angle of attack was determined using the onboard model AOA package and the roll potentiometer in the arc sector. For non-zero angle of sideslip runs, the AOA package and roll potentiometer in the arc sector were rotated through the Euler angles, which included sting dogleg angles and sting deflection angles, to determine model angle of attack and angle of sideslip. Tunnel upflow was also included in the final model angle of attack and angle of sideslip.

III.   Results and Discussion

This section discusses data analysis results from the wind tunnel test. The y-axis or z-axis scales have been removed from most of the plots due to SBU and ITAR restrictions. All plots within a figure are plotted

on the same scale for better comparison and interpretation.

III.A. Reynolds Number Effects

In the development of the aerodynamic database for the unpowered LAV, WT-to-flight scaling due to Reynolds number was managed as an uncertainty contribution. The results of a CFD analysis were used to construct a Reynolds number scaling term in the uncertainty buildup for the database, and it was one of the larger terms in the total level of uncertainty for the unpowered LAV. The CFD task, designated AR-75,[12] analyzed Reynolds number scaling on the previous LAV configuration (LAV-605-068) by examining the differences between a Reynolds number of 2.5 million and the flight values at Mach numbers of 0.3, 0.5, and 0.7. The data would have been more pertinent if it was focused on the ALAS-11-rev3c configuration, but at the time of the test, it was the only CFD data available that examined Reynolds number scaling on the LAV. Figure 18 shows a comparison between the LAV-605-068 configuration and the ALAS-11-rev3c configuration. The main differences lie in the design of the adapter cone and boost protective cover (BPC). The BPC for the ALAS-11-rev3c configuration was designed as an ogive to reduce high aeroacoustic loads at transonic and supersonic flight conditions. However, both configurations possess a sharp trailing edge near the CM shoulder that should help to reduce certain Reynolds number effects. The analysis had shown significant scaling effects at Mach 0.3, however, there were questions about the accuracy of the CFD solutions at that condition. The wind tunnel test provided data to assess whether the CFD predictions of Reynolds number effects on the LAV-605-068 configuration were also present on the ALAS-11-rev3c configuration.

Since the LAV can experience a wide range of Reynolds numbers during flight, the test team was interested in the spread of the aerodynamic coefficients over this range and how it compared to the pre-test CFD predictions. Figure 19 shows axial force coefficient data from the experiment at all tested Reynolds numbers. The spread in the data over the tested Reynolds number range is shown as a shaded region and the spread seems to be fairly constant with angle of attack. To give perspective, the magnitude of the spread is only 2-3% of the total C_A value. Figure 20 shows the same data as a function of Reynolds number. The trend with Reynolds number is either flat or exhibits a small linear slope. Finally, Fig. 21 shows the measured Reynolds number increment for C_A and compares it to the predicted Reynolds number increment from CFD. The measured Reynolds number increment from the test is calculated by finding the range (max - min) of C_A at each angle of attack. Also, there were CFD solutions for comparison only at Mach numbers of 0.3, 0.5, and 0.7. There is a large difference between the measured Reynolds number increment from the wind tunnel test and the predicted increment from CFD at Mach 0.3. The WT and CFD results compare much better at Mach 0.5 and 0.7, but the WT results still show a smaller Reynolds number effect than the CFD prediction. The balance accuracy and total unpowered LAV uncertainty from version 0.52.1 of the LAV aerodynamic database are also shown on the plots for comparison. The effect of Reynolds number on C_A as measured in the wind tunnel test is sometimes below the balance accuracy, but it is much smaller than the database uncertainty.

Similar plots are shown for normal force coefficient in Figs. 22-24 and for pitching moment coefficient in Figs. 25-27. The spread in C_N over the tested Reynolds number range is very small when compared to the total magnitude of C_N (Fig. 22). Furthermore, the trends with Reynolds number are almost flat, suggesting that Reynolds number has little to no effect on C_N (Fig. 23). Similar to C_A, the measured Reynolds number effects on C_N from the WT test are much smaller than the CFD predicted effect at Mach 0.3 (Fig. 24) and agree more closely at Mach 0.5 and 0.7. Finally, for pitching moment coefficient, the data spread across the tested Reynolds number range is also small when compared to the total magnitude of C_m (Fig. 25). There is more spread in the data at Mach 0.3 and 0.7 than the other Mach numbers, and at Mach 0.9 and 0.95, the spread at angles of attack greater than 15° deviates from the trend at the lower angles of attack. Fig. 26 shows that at Mach 0.3 and 0.7, there is a slight minimum in C_m at 20 million Reynolds number, which is not seen at the other Mach numbers. At Mach 0.9, there is a decreasing linear trend with Reynolds number for angles of attack above 15°. Comparing the measured Reynolds number effect on C_m against CFD results also shows a large difference at Mach 0.3 (Fig. 27) and closer agreement at Mach 0.5 and 0.7.

Overall, the results show small effects of Reynolds number on the unpowered LAV when compared to the database uncertainty, CFD predictions, and the total magnitude of the coefficient. The CFD predictions showed large Reynolds number scaling increments at Mach 0.3 and did not compare well to the measured Reynolds number increments from the wind tunnel test. This result was not consistent with the results at Mach 0.5 and 0.7, and it is not clear whether this is caused by the differences between the two LAV configurations or if there were problems with the CFD solutions at Mach 0.3. The results from the test can

help to refine CFD on blunt body vehicles and help with predictions of Reynolds number effects for vehicles with sharp trailing edges.

III.B. CFD Validation Exercise

A post-test CFD validation exercise was conducted using CFD numerical simulations performed for the unpowered LAV (ALAS-11-rev3c configuration) at the highest Reynolds numbers achieved during the wind tunnel test. Using the OVERset grid FLOW solver (OVERFLOW[13]), the CFD task, designated AR-119,[14] provided force and moment comparison data. The tunnel walls were not simulated in the CFD analyses, but the model support sting used in the wind tunnel test was simulated, and a correction to axial force was applied similar to the process used in the wind tunnel test. Solutions were obtained at angles of attack between -20° and 20° for zero angle of sideslip only. The CFD solutions provided comparisons only at the highest Reynolds number conditions reached at each Mach number during the WT test. Most of the solutions converged to a steady-state value, but there were some cases that required time-accurate iterations to resolve the flow features and properly simulate the environment.

In general, the CFD solutions compared well to the wind tunnel data for normal force and pitching moment coefficients (Figs. 28, 29). The balance accuracy is shown as a shaded band around the wind tunnel data. There is a small difference in C_N and C_m between 0° and 10° angles of attack at Mach 0.5 and 0.7. Also, there is a slight difference in C_m at the higher angles of attack (> 15°) for Mach 0.9 and 0.95. The longitudinal static pressure rows also show good comparison between the WT and CFD results at all conditions available. With the limited number of pressure orifices on the model, there are no features that stand out in the pressure comparisons to explain the small differences seen in C_N and C_m. Figure 30 shows example pressure comparisons at $\alpha = 10°$ for the longitudinal pressure row at $\phi=90°$.

For axial force coefficient, however, the CFD solutions did not compare well to the wind tunnel data, especially at the subsonic Mach numbers (Fig. 31). The CFD team believes the results show a deficiency in the code's ability to capture drag on a vehicle with a large separated wake using the current available turbulence models.[14] For the LAV, the base drag is a larger component of the total drag than skin friction drag. The reason for the large difference in axial force coefficient between wind tunnel and CFD results may lie in the differences in base pressures. The base contribution to the total axial force coefficient may be approximated by

$$\hat{C}_{A_{base}} = \bar{C}_{p_{base}} \left(\frac{A_{base}}{S_{ref}} \right) \tag{1}$$

where $\bar{C}_{p_{base}}$ is an average pressure coefficient over the base area. For the LAV, A_{base} is equal to S_{ref} (area based on CM heat shield diameter). Therefore, the difference in the base contribution to the total axial force coefficient between wind tunnel and CFD results can be estimated as the difference in base pressure coefficients. This approximation is used because there were not enough pressure taps on the base of the wind tunnel model to allow for direct integration of pressures.

$$\left(\Delta \hat{C}_{A_{base}} \right)_{WT-CFD} = \left(\Delta \bar{C}_{p_{base}} \right)_{WT-CFD} \tag{2}$$

The plots in Fig. 31 show that the difference in axial force coefficient between wind tunnel and CFD results decreases with increasing Mach number. At Mach 0.9, the two data curves almost line up. Focusing on $\alpha=0°$, the base pressure coefficients between WT and CFD results are plotted for three radial pressure rows on the CM heat shield in Figs. 32-34. The measured base pressure coefficients from the test stay at a nearly constant value for every Mach number, but the CFD results show a much larger variation with Mach number. For the inner ring at r/D = 0.231 (Fig. 32), the C_p values are consistently different between WT and CFD, and it follows the same trend seen in C_A (i.e., the differences decrease with increasing Mach number). For the middle and outer rings at r/D = 0.410 and r/D = 0.473, respectively, the differences are not as large, but are still evident.

There were not enough pressure taps to accurately determine the average C_p difference between WT and CFD over the entire base area. However, with the few pressure taps available, an estimate of $\left(\Delta \bar{C}_{p_{base}} \right)_{WT-CFD}$ can be made. For example, at Mach 0.3, the average C_p difference between the WT and CFD results is calculated to be 0.056 using the C_p data from the three rings. This value is about the same magnitude as the difference seen in C_A (= 0.053) at Mach 0.3 and $\alpha=0°$ (Fig. 31), suggesting that the differences in C_A come mainly from the differences in the base drag between WT and CFD results.

III.C.   Database Uncertainty Reduction

One of the outcomes of the test was the reduction of axial force coefficient uncertainty for the unpowered LAV in the aerodynamic database. Database version 0.52.1 included a WT-to-flight scaling uncertainty due to Reynolds number derived from the results of the CFD analysis (AR-75) discussed earlier. The analysis showed large increments due to Reynolds number for axial force coefficient (Fig. 21), especially at Mach 0.3. The data from this wind tunnel test showed that the difference in C_A between low and flight Reynolds numbers was much smaller than the CFD prediction. As a result, the uncertainty term for scaling wind tunnel data to flight was significantly reduced.

Another reason for the reduction in axial force coefficient uncertainty was the excellent data repeatability exhibited during the test. Repeat runs were randomized throughout the matrix to cover as many test conditions as possible. Some repeats were back-to-back runs, while others were taken hours or days later. The intent of these runs was to measure the level of data repeatability for the test setup (tunnel, model, balance). The analysis for determining the data repeatability levels follows techniques employed in statistical process control.[15, 16] For each set of repeat runs, the runs are first interpolated to nominal angle of attack values. Then, an average is calculated at each nominal angle of attack as well as residuals of each run from that average. The range (max-min) of the residuals is divided by a number (d_2) that relates the mean range of samples from a normal distribution to its standard deviation. This number has different values depending on the number of samples. The average range of the residuals across the angles of attack divided by d_2 provides an unbiased estimate of the standard deviation of the test setup. These estimates can then be grouped according to different independent variables such as Mach number to discern trends. The overall repeatability metrics for the test are shown in Table 2.

Table 2.   Data repeatability standard deviation estimates.

Coefficient	Repeatability Estimate (1σ)
C_A	0.0012
C_N	0.0020
C_m	0.0010
C_Y	0.0018
C_n	0.0008
C_l	0.0003

Database version 0.52.1 used data from a test at another wind tunnel facility. The data repeatability levels for C_A from that test were significantly larger, especially for the subsonic Mach numbers, whereas, the levels for the other coefficients were similar between the two tests. The reason for the large difference is speculated to be caused by differences in the quality of the axial force gauge on the two balances or simply differences between the two tunnels. Figure 35 shows the comparison of repeatability levels for C_A between the two wind tunnel tests. The balance accuracies from each test are also shown for comparison. The repeatability levels from this WT test (identified as WT test 83-AA) were significantly lower than the previous test (identified as WT test 75-AA) and this contributed to the lowering of the total database C_A uncertainty for the unpowered LAV.

Finally, Fig. 36 shows the comparison of the total C_A uncertainty for the unpowered LAV between the previous database (V0.52.1) and the database (V0.53) that incorporated the data from this wind tunnel test. The C_A uncertainty level was reduced significantly, with nearly an order of magnitude reduction at Mach 0.5 and 0.7.

IV.   Concluding Remarks

A wind tunnel investigation of Reynolds number effects on the ALAS-11-rev3c configuration of the Orion Launch Abort Vehicle was conducted in the NASA Langley National Transonic Facility in early 2009. Static aerodynamic force and moment as well as static pressure data were obtained on the 6%-scale model of the LAV at flight Reynolds numbers at Mach numbers between 0.3 and 0.95 for angles of attack from -4 to +22 degrees and angles of sideslip from -10 to +10 degrees. Data were also obtained at various intermediate

Reynolds numbers (from 2.5 million to 45 million based on CM heat shield diameter) in order to examine the effects of Reynolds number on the vehicle.

The test results demonstrated that Reynolds number effects on the unpowered ALAS-11-rev3c configuration are small when compared to the total database uncertainty and to pre-test CFD predictions. Results of a CFD validation exercise suggests that the differences seen in axial force coefficient may be associated with inaccurate CFD predictions of base drag. An important outcome of the test was the significant reduction of the total database uncertainty on axial force coefficient. This was accomplished because of good data repeatability during the test and because of reaching flight Reynolds numbers which decreased the uncertainty on scaling wind tunnel data to flight.

Acknowledgments

References

[1] NASA, "http://www.nasa.gov/mission_pages/constellation/orion," .

[2] Om, D., Curtin, M. M., Bogue, D. R., Witkowski, D. P., and Ball, D. N., "Reynolds Number Effects on a Subsonic Transport at Transonic Conditions (Invited)," AIAA Paper 2001-0909, 2001.

[3] Wahls, R. A., Owens, L. R., and Rivers, S. M. B., "Reynolds Number Effects on a Supersonic Transport at Transonic Conditions (Invited)," AIAA Paper 2001-0912, 2001.

[4] Fuller, D., Gloss, B., and Nystrom, D., "Guide for Users of the National Transonic Facility," NASA TM 83124, July 1981.

[5] Braslow, A., Hicks, R., and Harris, Jr., R., "Use of Grit-Type Boundary-Layer-Transition Trips on Wind-Tunnel Models," NASA-TN D-3579, 1966.

[6] Braslow, A. and Knox, E., "Simplified method for determination of critical height of distributed roughness particles for boundary-layer transition at Mach numbers from 0 to 5," NACA-TN 4363, 1958.

[7] Kilgore, W. A., Balakrishna, S., and Butler, D. H., "Reduction of Tunnel Dynamics at the National Transonic Facility (Invited)," AIAA Paper 2001-1162, 2001.

[8] Robinson, P. E. and A.Thompson, J., "Formulation of the Orion Aerodynamic Database," CEV Aerosciences Project, Rept. EG-CEV-06-37, NASA Johnson Space Center, Houston, TX, Mar. 2011.

[9] Foster, J. and Adcock, J., "User's Guide for the National Transonic Facility Research Data System," NASA Technical Memorandum 110242, April 1996.

[10] Ulbrich, N. and Boone, A., "Direct Validation of the Wall Interference Correction System of the Ames 11-Foot Transonic Wind Tunnel," May 2003, NASA/TM-2003-212268.

[11] Walker, E., "Statistical Calibration and Validation of a Homogeneous Ventilated Wall-Interference Correction Method for the National Transonic Facility," NASA/TP 2005-213947, 2005.

[12] Vicker, D. J., Greathouse, J., and Stuart, P., "LAV-605-068 ACM Wind Tunnel to Flight Extrapolation Assessment using OVERFLOW," CEV Aerosciences Project, Rept. EG-CAP-08-25, NASA Johnson Space Center, Houston, TX, Jun. 2007.

[13] Nichols, R. H. and Buning, P. G., *User's Manual for OVERFLOW 2.1*, version 2.1t ed., August 2008.

[14] Schwing, A., "OVERFLOW Analysis for LAV Geometry Corrections," CEV Aerosciences Project, Rept. EG-CAP-11-03, NASA Johnson Space Center, Houston, TX, Aug 2010.

[15] Wheeler, D. and Chambers, D., *Understanding Statistical Process Control*, SPC Press, Knoxville, 2nd ed., 1992.

[16] Wheeler, D., *Advanced Topics in Statistical Process Control*, SPC Press, Knoxville, 1995.
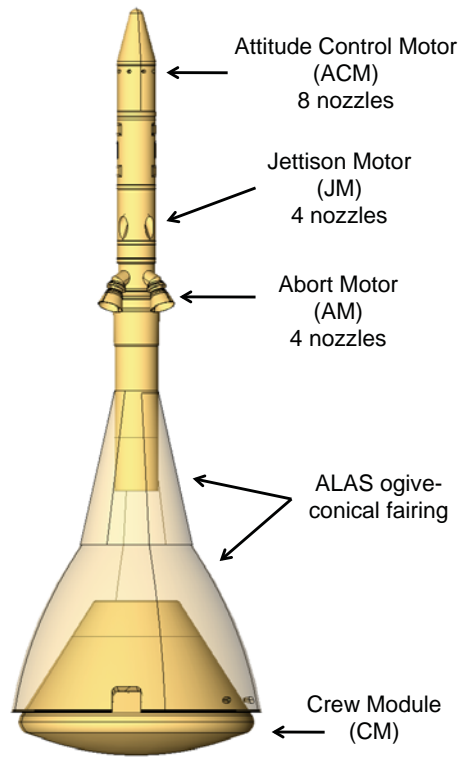
Figure 1. Orion Launch Abort Vehicle.

Attitude Control Motor
(ACM)
8 nozzles

Jettison Motor
(JM)
4 nozzles

Abort Motor
(AM)
4 nozzles

ALAS ogive-
conical fairing

Crew Module
(CM)
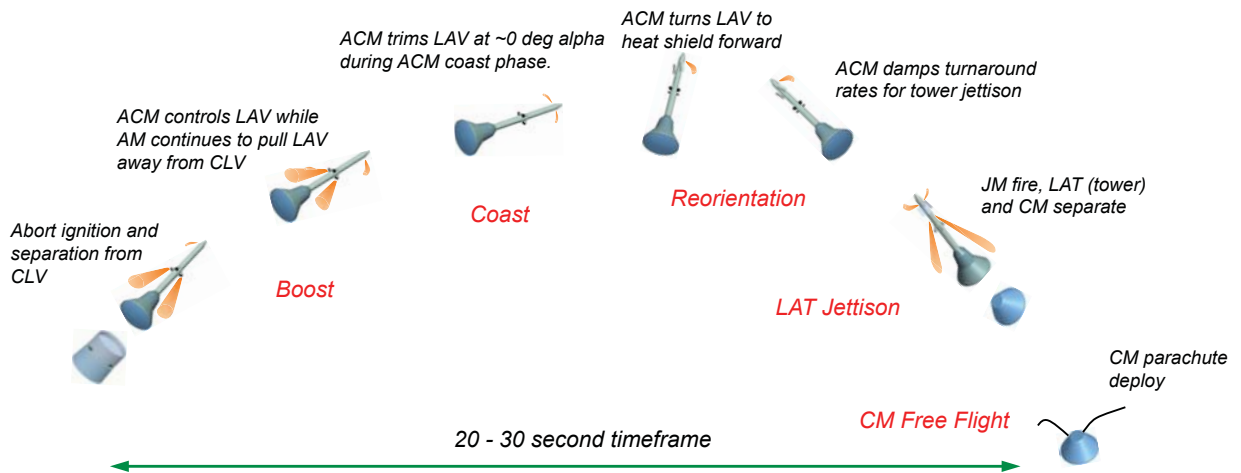
Figure 2. Phases of LAV abort sequence.

ACM trims LAV at ~0 deg alpha
during ACM coast phase.

ACM turns LAV to
heat shield forward

ACM damps turnaround
rates for tower jettison

ACM controls LAV while
AM continues to pull LAV
away from CLV

Coast

Reorientation

JM fire, LAT (tower)
and CM separate

Abort ignition and
separation from
CLV

Boost

LAT Jettison

CM parachute
deploy

CM Free Flight

20 - 30 second timeframe

American Institute of Aeronautics and Astronautics

Figure 3. Flight trajectory simulation showing expected Reynolds number range for the LAV for various ascent abort scenarios.
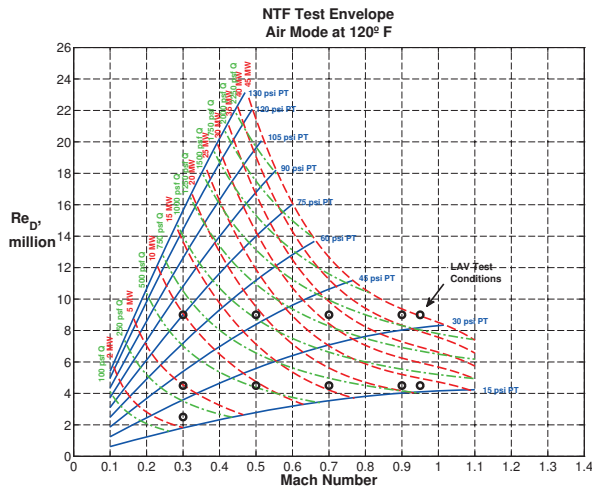
(a) Air mode operating envelope at 120 °F
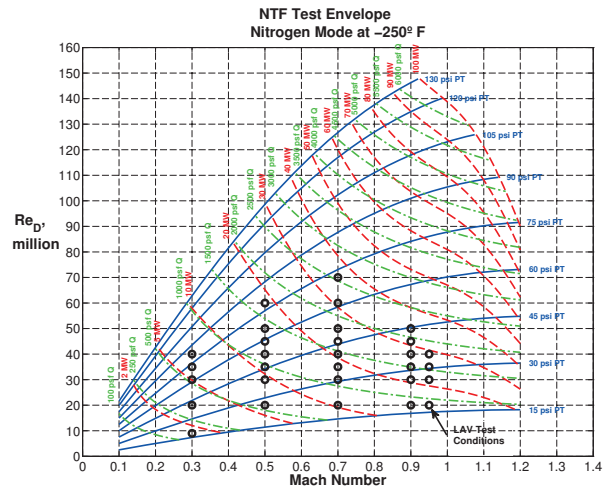
(b) Nitrogen mode operating envelope at -250 °F

Figure 4. NTF operating envelopes.
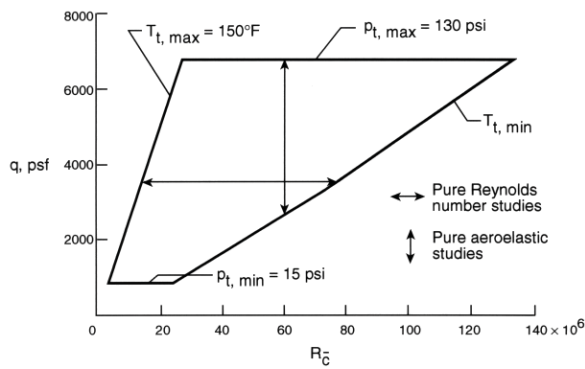
(a) Constant Mach number
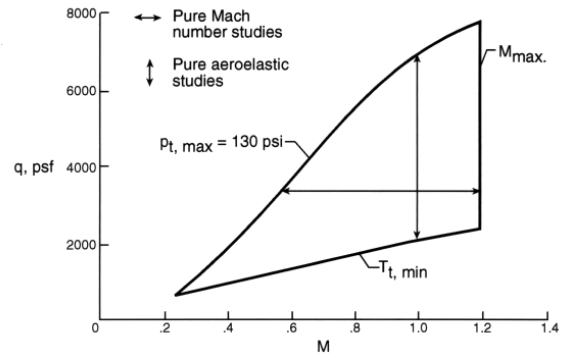
(b) Constant Reynolds number
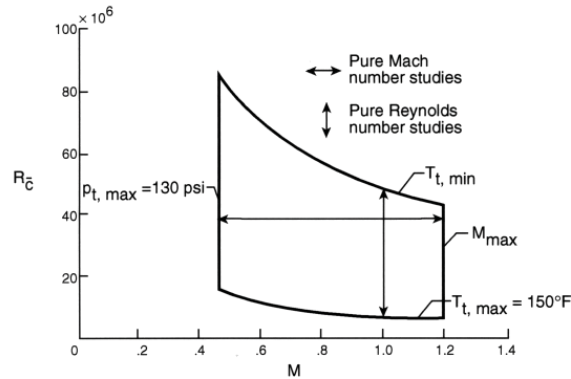
(c) Constant dynamic pressure

Figure 5. Unique capability of NTF to isolate Mach, Reynolds number, and aeroelastic effects.

Mach	Re_D (million)											
Number	2.5	4.5	9	9	20	30	35	40	45	50	60	70
0.3	X	X	X	X	X			X				
0.5		X	X		X			X			X	
0.7		X	X		X			X				X
0.9		X	X		X			X		X		
0.95		X	X		X	X		X				
1.05		X	X		X	X	X					
1.1		X			X	X						

AIR   **NITROGEN**

Figure 6. Pre-test matrix.

American Institute of Aeronautics and Astronautics
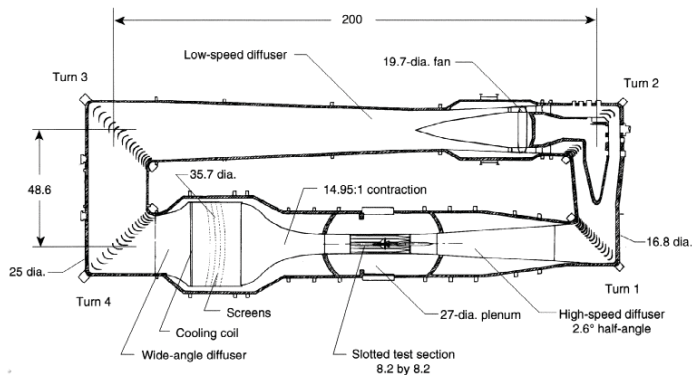
(a) NTF tunnel circuit
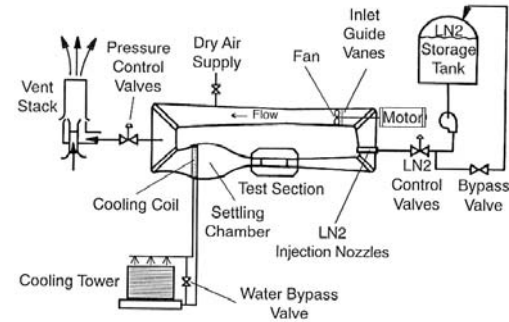
(b) NTF operational schematic
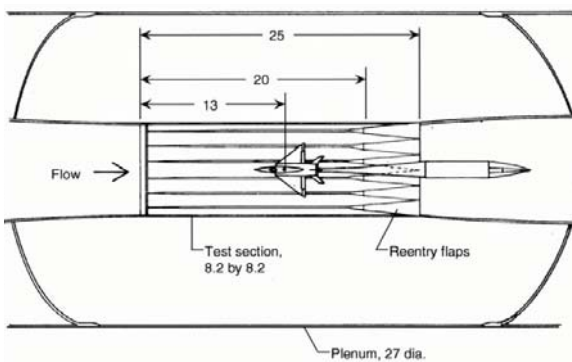
(c) NTF test section

(d) NTF LN$_2$ injectors

Figure 7. Overview of the National Transonic Facility.

Index	Model Component
1	Tower Nose
2	Tower + ALAS Cone
3	Raceway
4	AM Nozzles (4)
5	Balance Adapter
6	ALAS Ogive
7	Umbilical Filler
8	CM Heat Shield Halves (2)
9	NTF-118 Balance
10	NTF AOA Package
11	AOA Plate
12	ESP Heated Enclosures
13	Leveling Plate
14	Sting
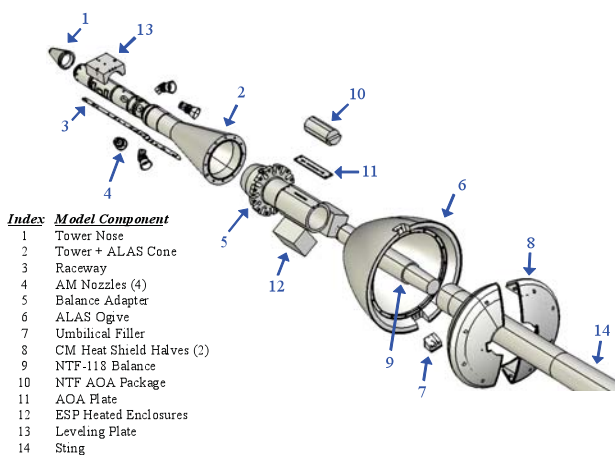
(a) Exploded view of LAV model
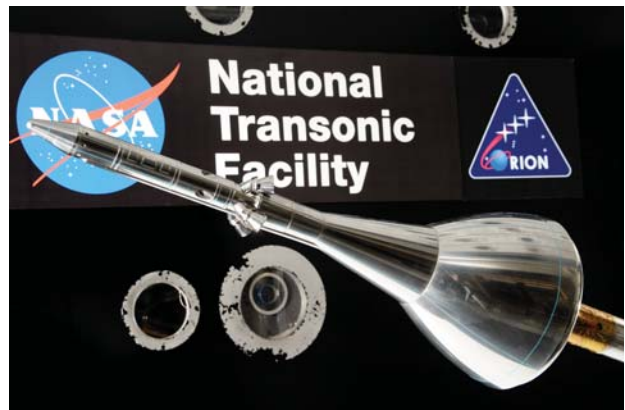
(b) Photo of LAV model in the NTF

Figure 8. Details of Orion LAV model tested in the NTF.

(a) Longitudinal view

CM Heat Shield

CM Bumper
(Back of ALAS Ogive)

Rear of Tower,
ALAS Cone & Ogive

Front of Tower

All Rear Views

Rear of Tower	ALAS Cone	ALAS Ogive
R/D = 0.082	R/D = 0.103	R/D = 0.255
R/D = 0.097	R/D = 0.125	R/D = 0.288
R/D = 0.092	R/D = 0.147	R/D = 0.318
	R/D = 0.192	R/D = 0.373
	R/D = 0.222	R/D = 0.460
	R/D = 0.233	R/D = 0.517
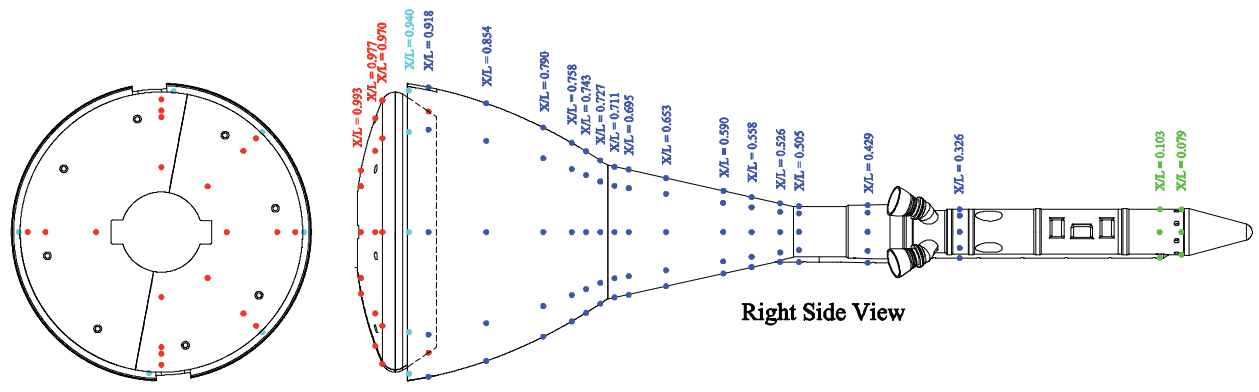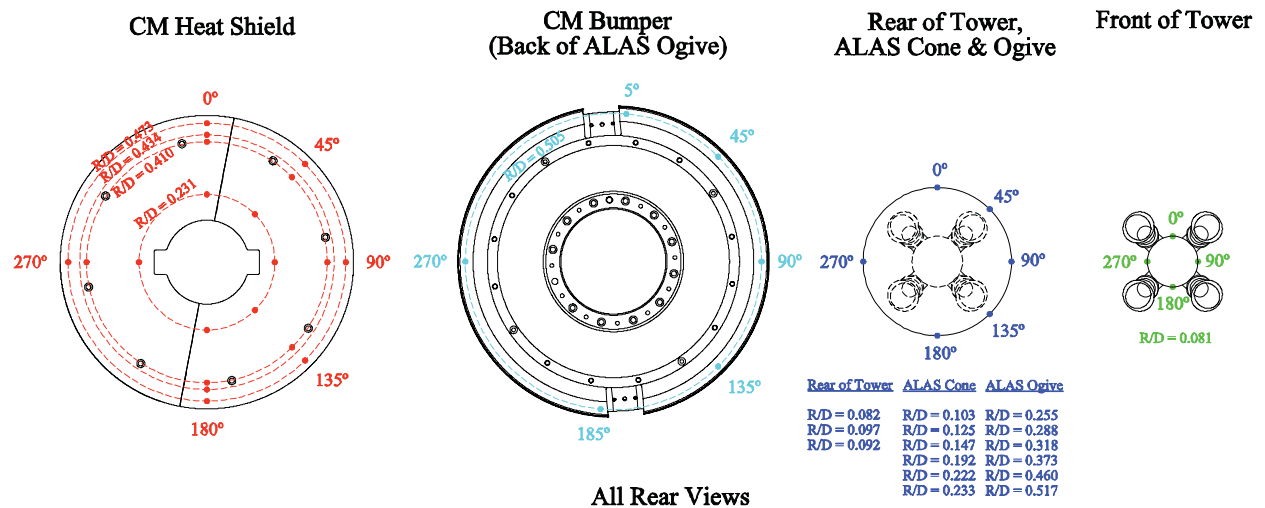
(b) Radial view

Figure 9. Static pressure port layout.
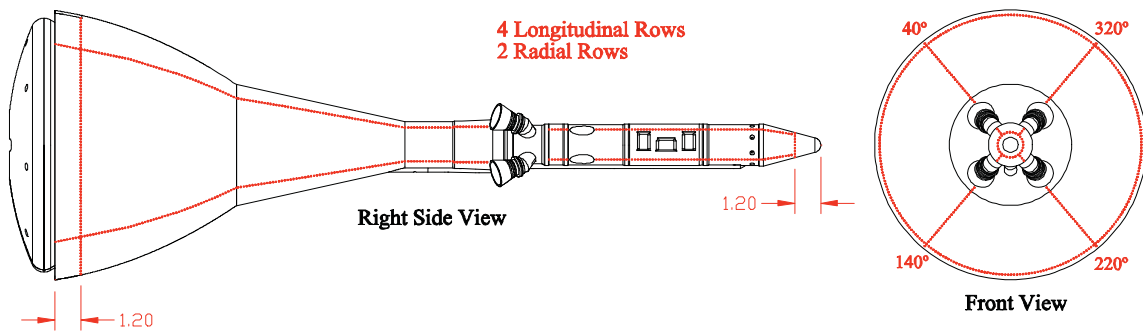
Figure 10. Boundary layer transition scheme used on the LAV model for low Reynolds number runs.
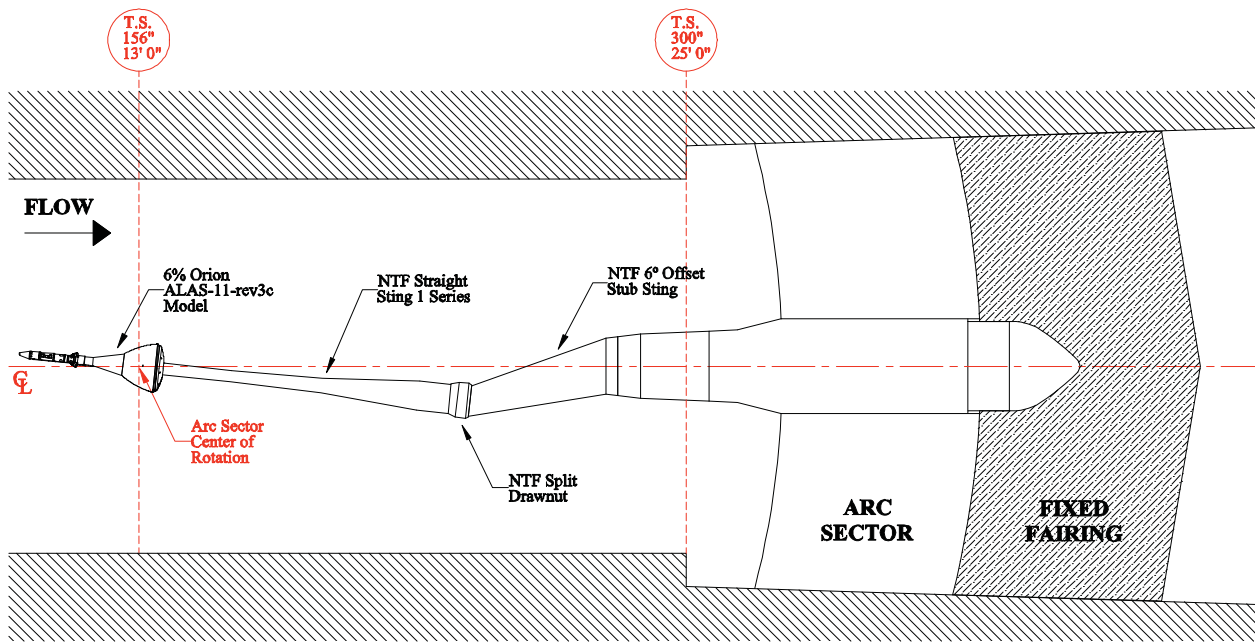
(a) Test section assembly sketch
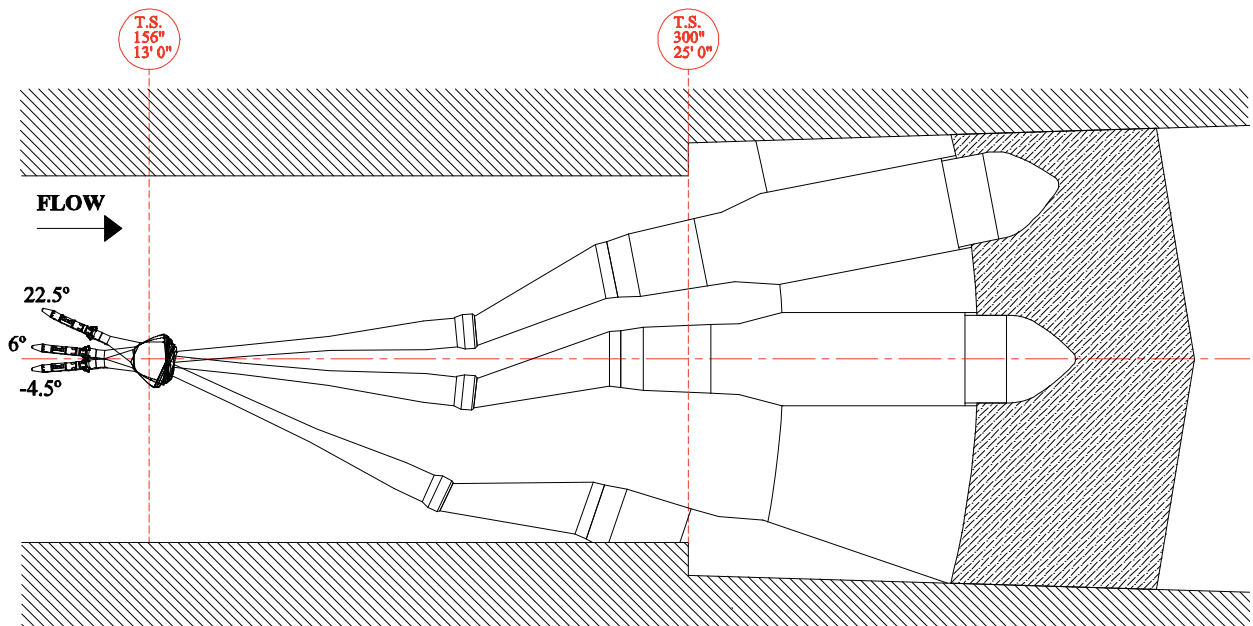
(b) Model location in test section with angle of attack

Figure 11. 6%-scale Orion LAV model installed in NTF test section.
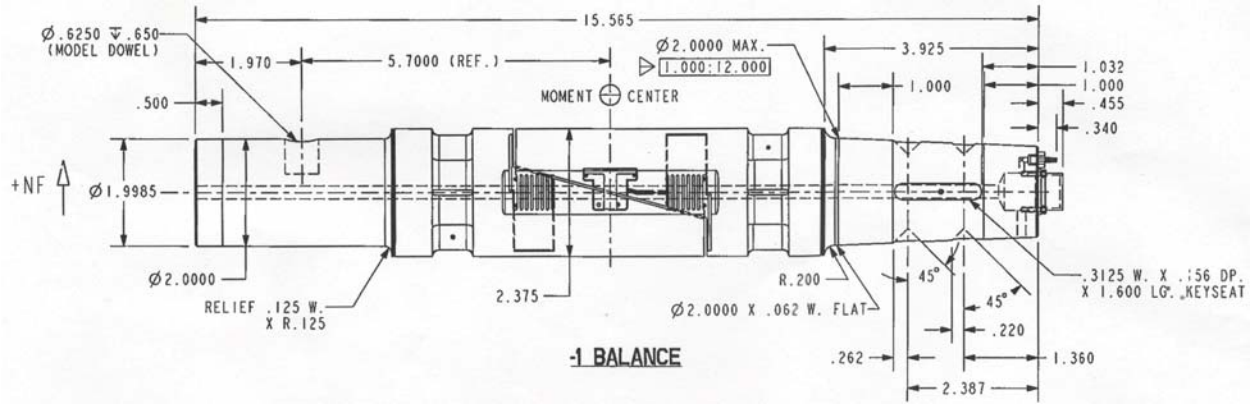
Figure 12. Outline drawing of NTF-118A strain gauge balance.

(a) Outline drawing

(b) Package location in model
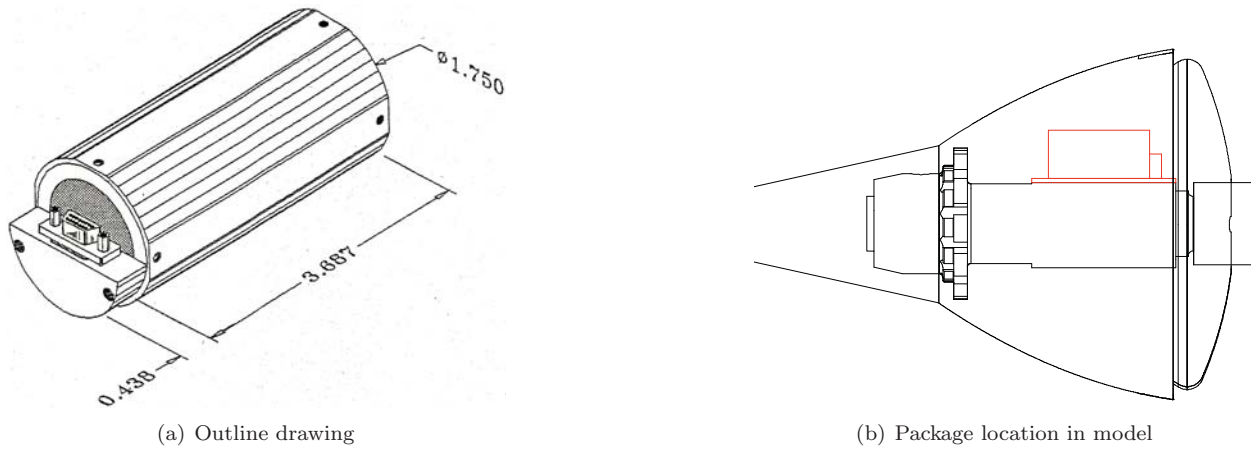
Figure 13. Details of NTF 204 series AOA package.
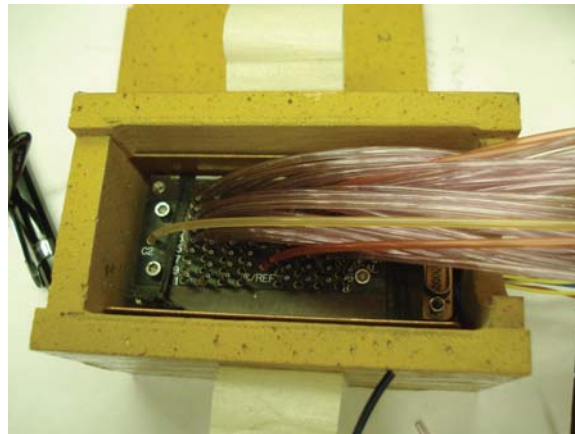
Figure 14. ESP package inside of insulated heated enclosure.
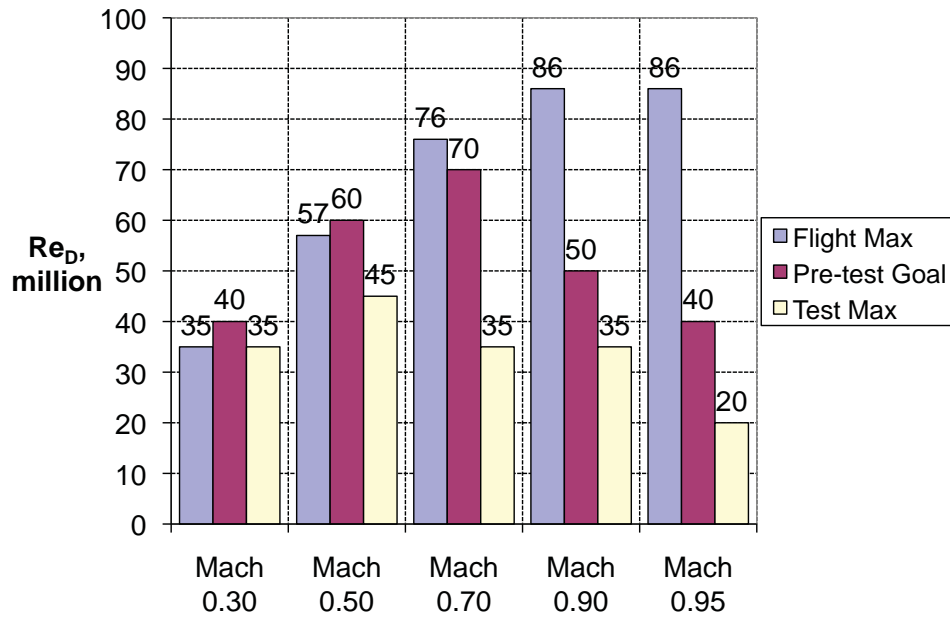
Figure 15. Summary of Reynolds number coverage for the test.

Mach Number	Re$_D$ (million)							
	2.5	4.5	9	20	30	35	40	45
0.3		-10		-10	-10			
	0	0	0	0	0	0		
		5		5	5			
	10	10	10	10	10	10		
0.5		-10		-10				
		0	0	0			0	
		5		5				
		10	10	10			10	10
0.7		-10		-10	-10	-10		
		0	0	0	0	0		
		5		5				
		10	10	10		10		
0.9		-10		-10		-10		
		0	0	0		0		
		5		5				
		10	10	10				
0.95		-10		-10				
		0	0	0				
		5		5				
		10	10	10				
1.05								
1.1								

-10	
0	Sideslip Angle (β)
5	
10	

Figure 16. Reynolds number and sideslip angle coverage from test.

American Institute of Aeronautics and Astronautics
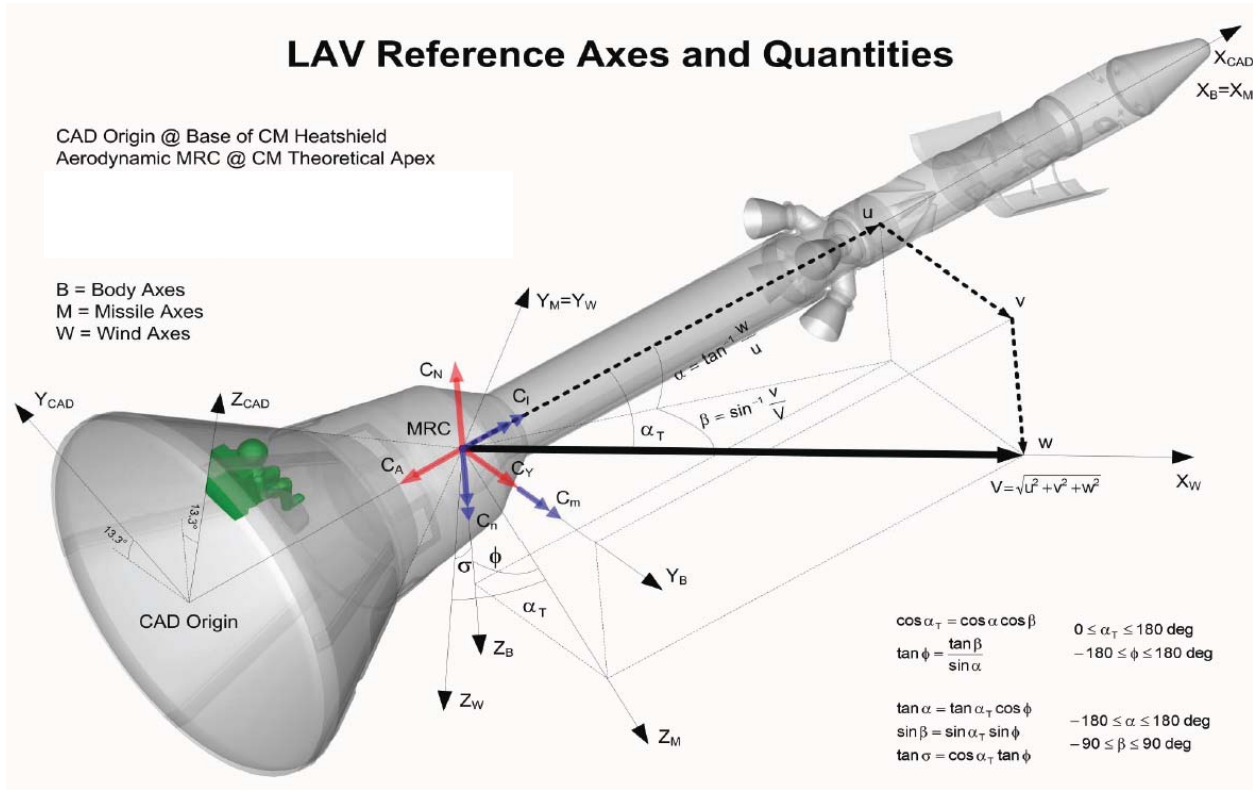
(a) Axes system definitions and sign conventions
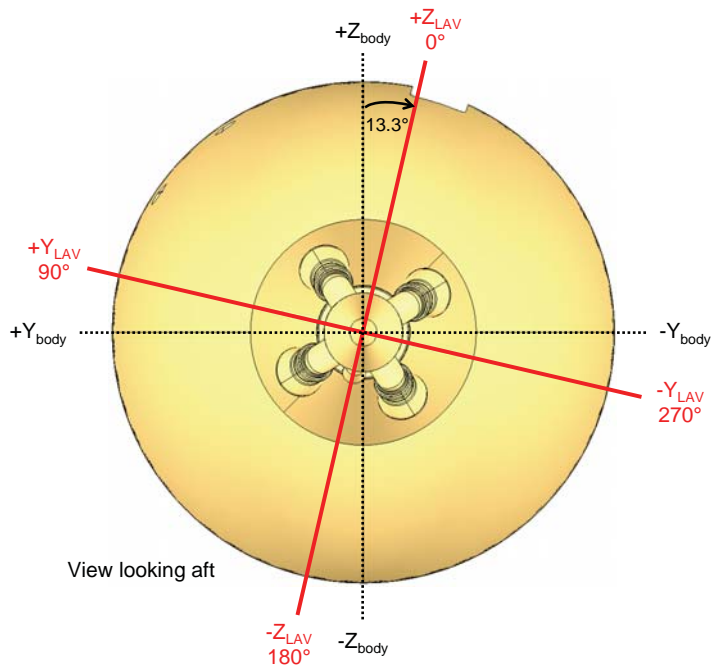
(b) LAV aerodynamic coordinate system
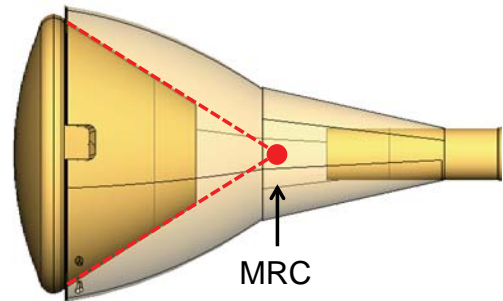
(c) Moment Reference Center (MRC) location

Figure 17. LAV axes system and definitions.

LAV-605-068 **ALAS-11-rev3c**

Adapter
Cone

Boost
Protective
Cover

Sharp edge
around shoulder
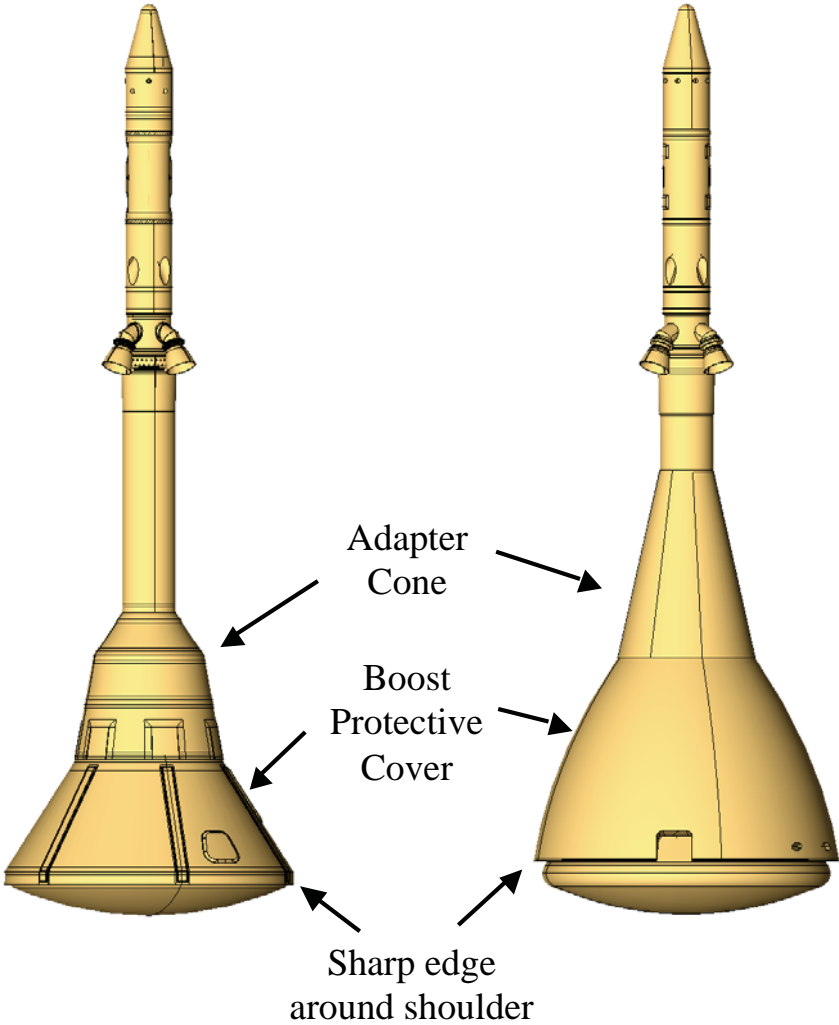
Figure 18. Comparison of two configurations of the LAV.

American Institute of Aeronautics and Astronautics
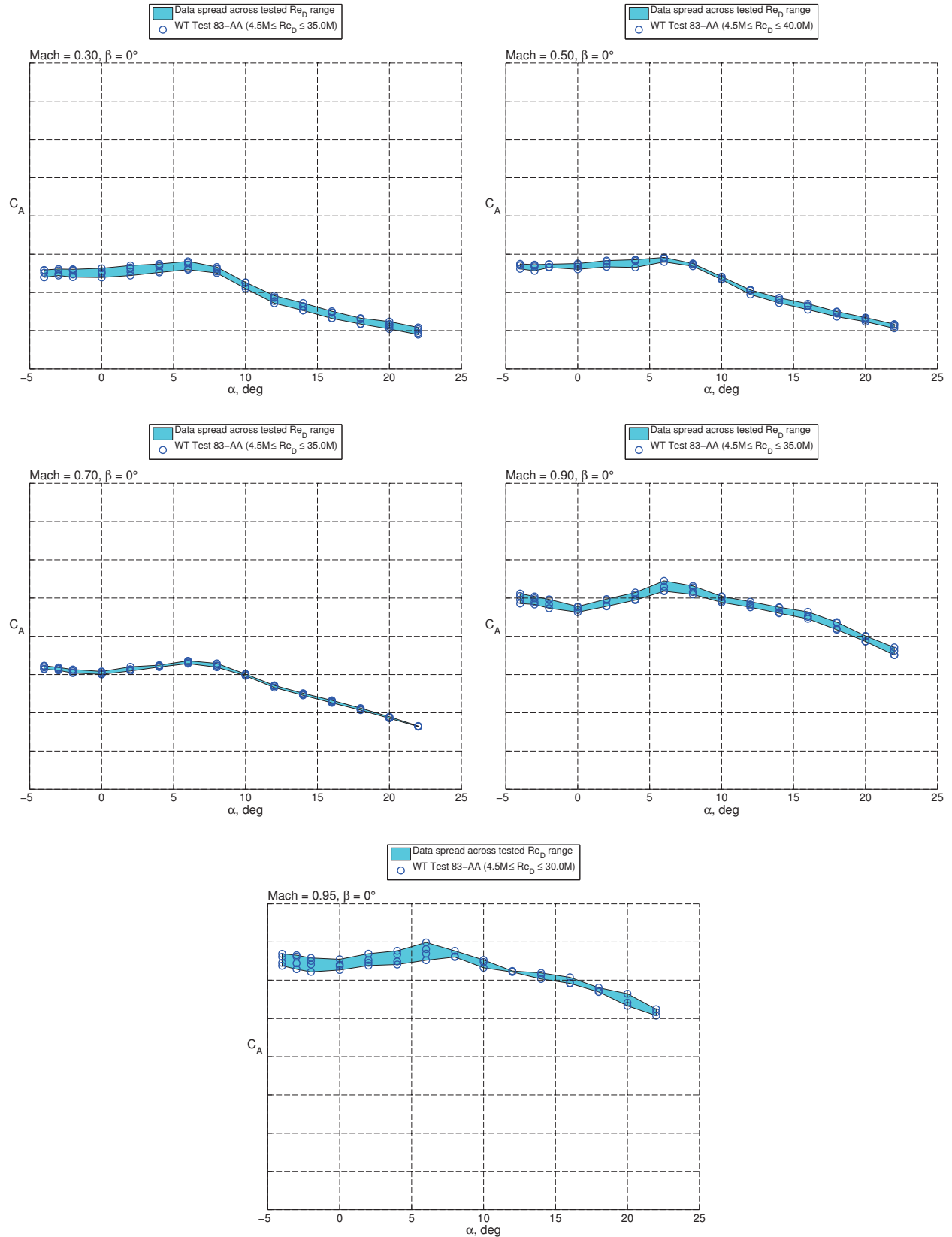
Figure 19. Data spread in axial force coefficient across tested Reynolds number range.

American Institute of Aeronautics and Astronautics
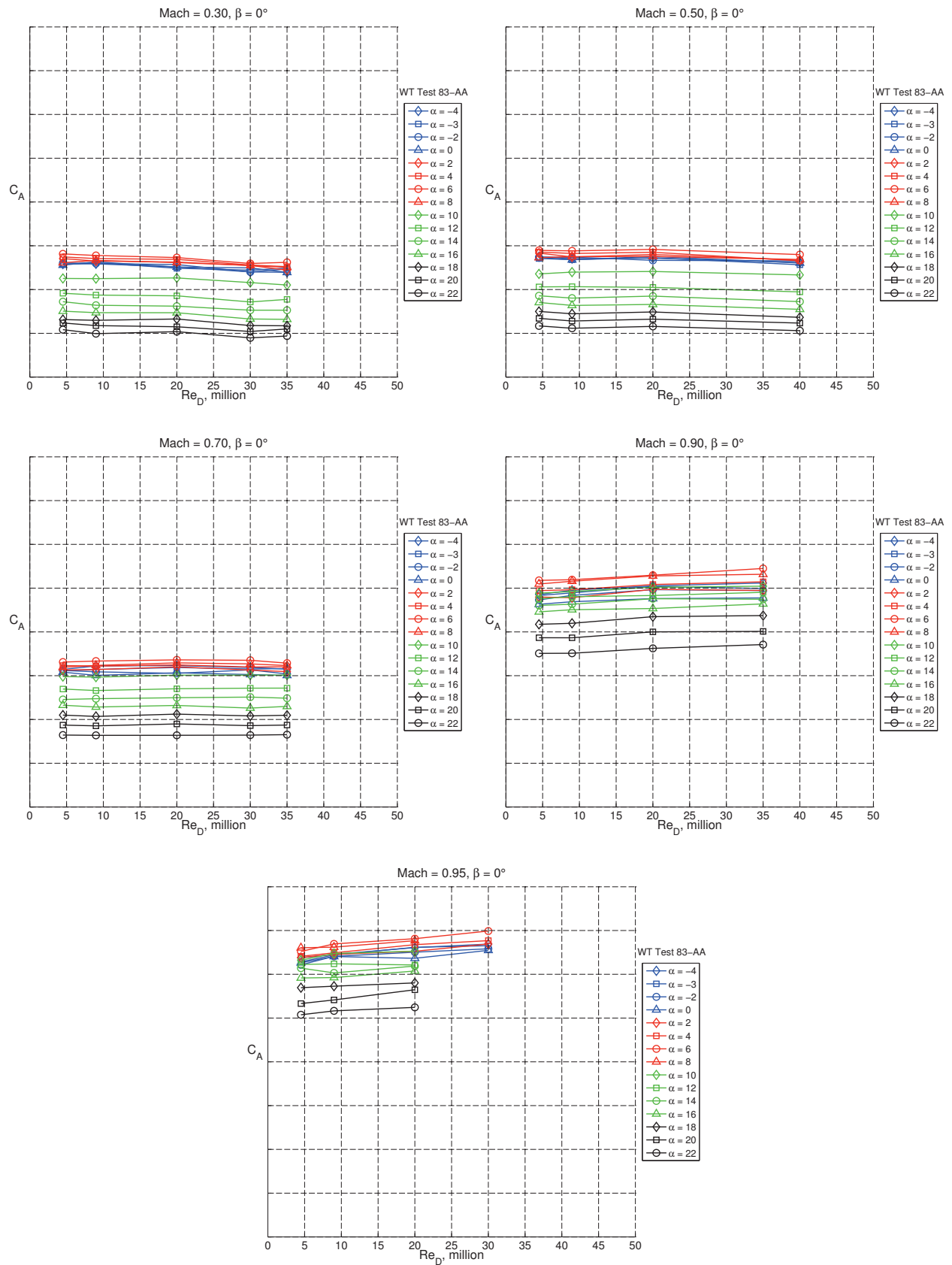
Figure 20. Trend in axial force coefficient with Reynolds number.
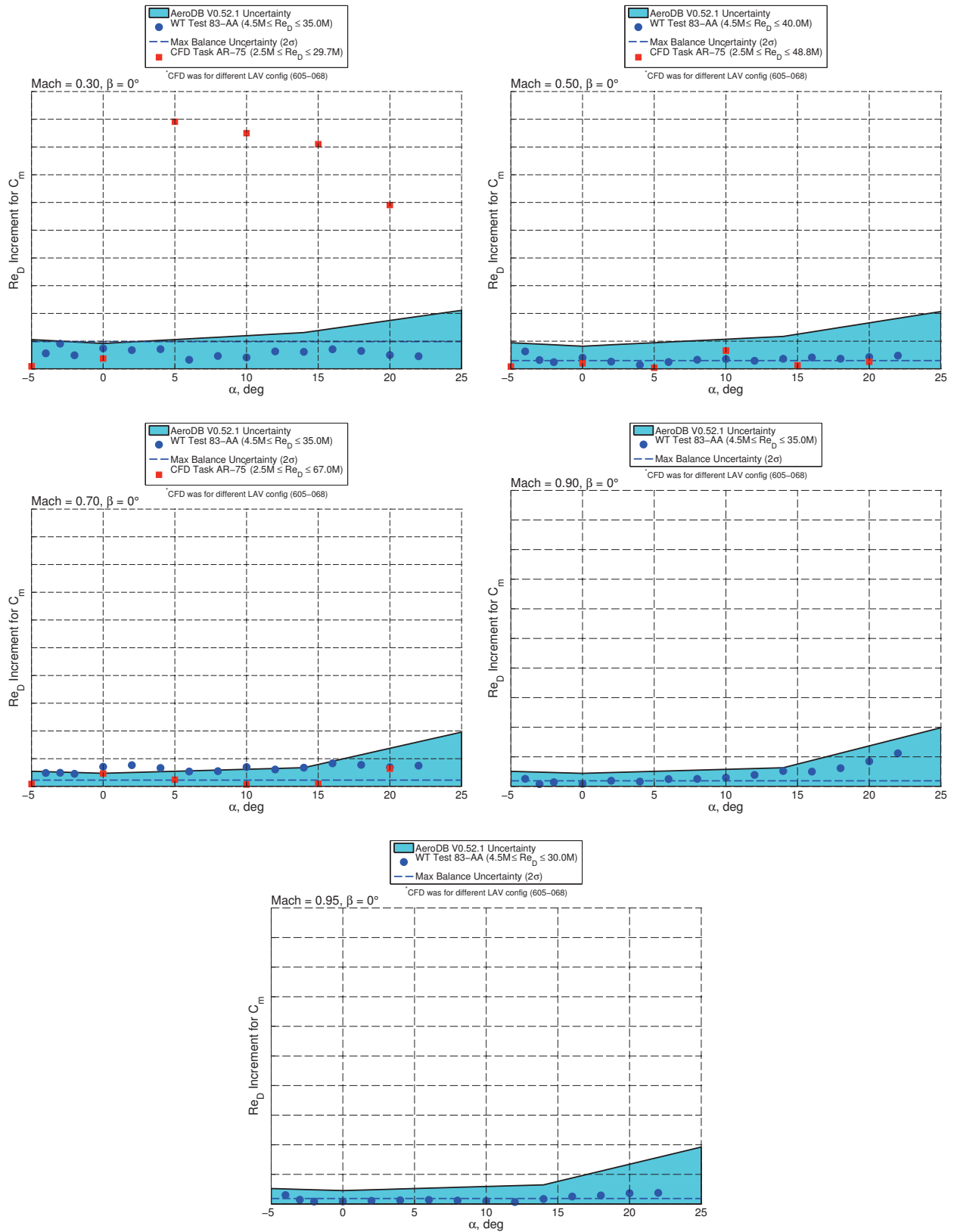
American Institute of Aeronautics and Astronautics
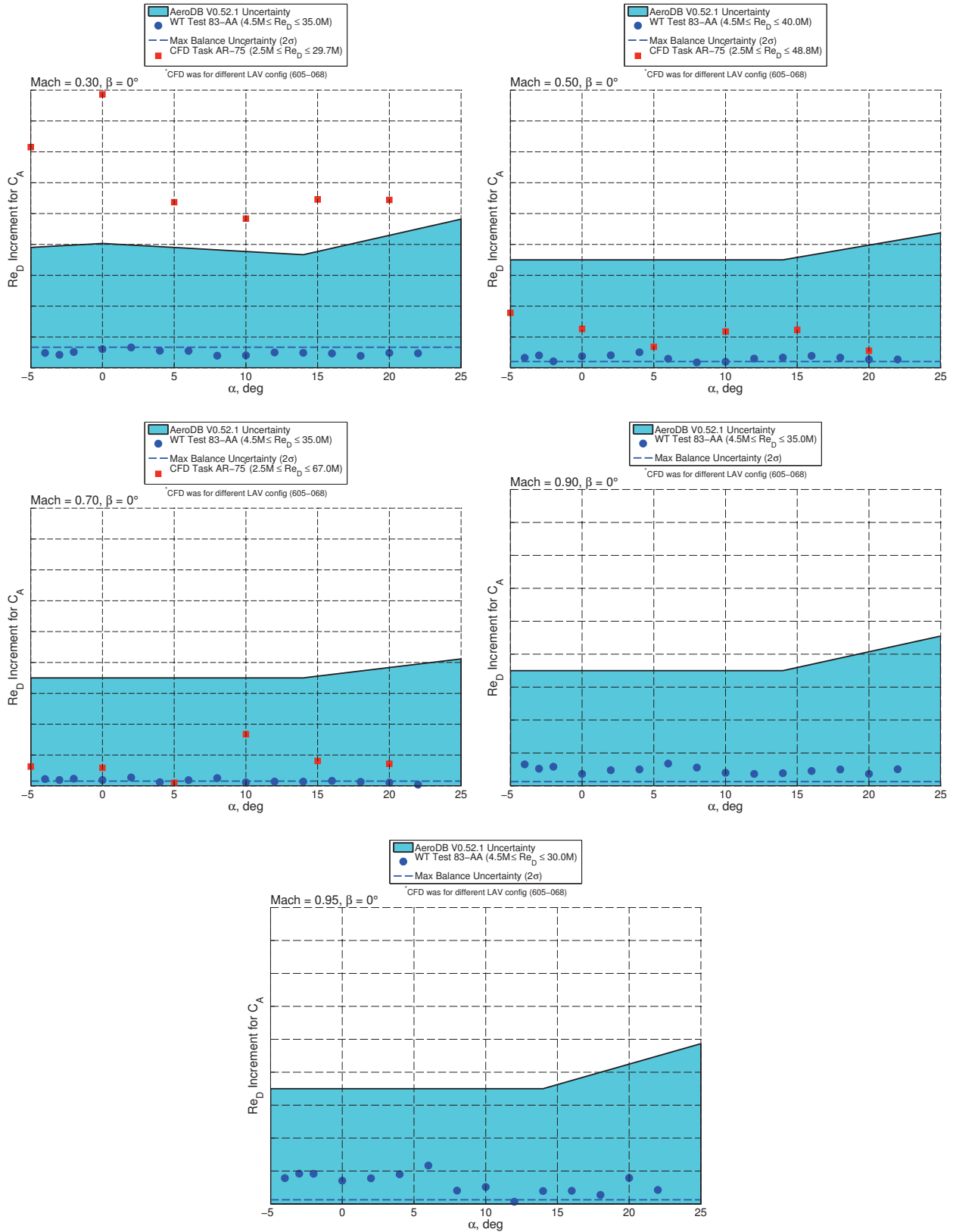
Figure 21. **Comparison between wind tunnel data and CFD of the range in axial force coefficient over Reynolds number range.**
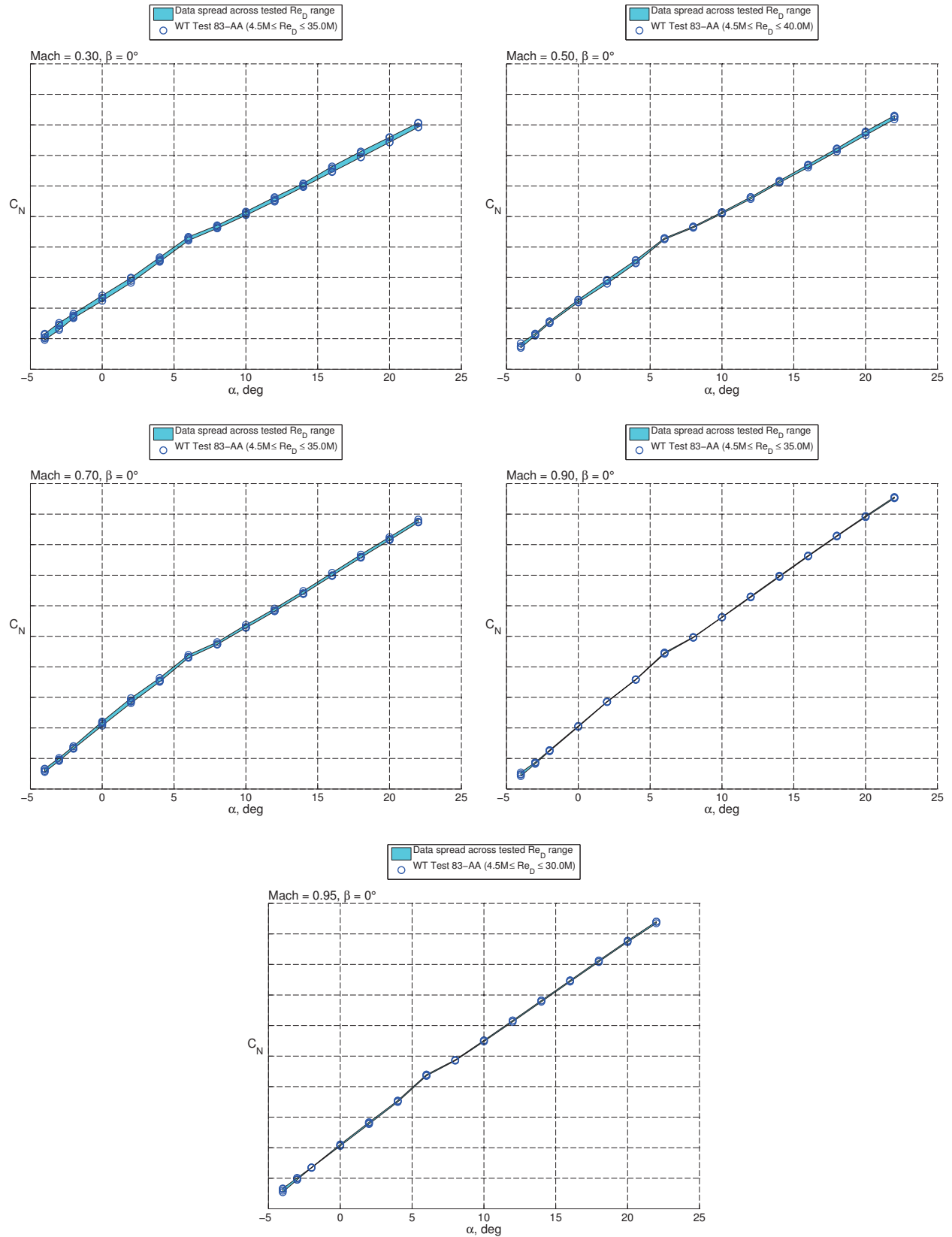
Figure 22. Data spread in normal force coefficient across tested Reynolds number range.

American Institute of Aeronautics and Astronautics
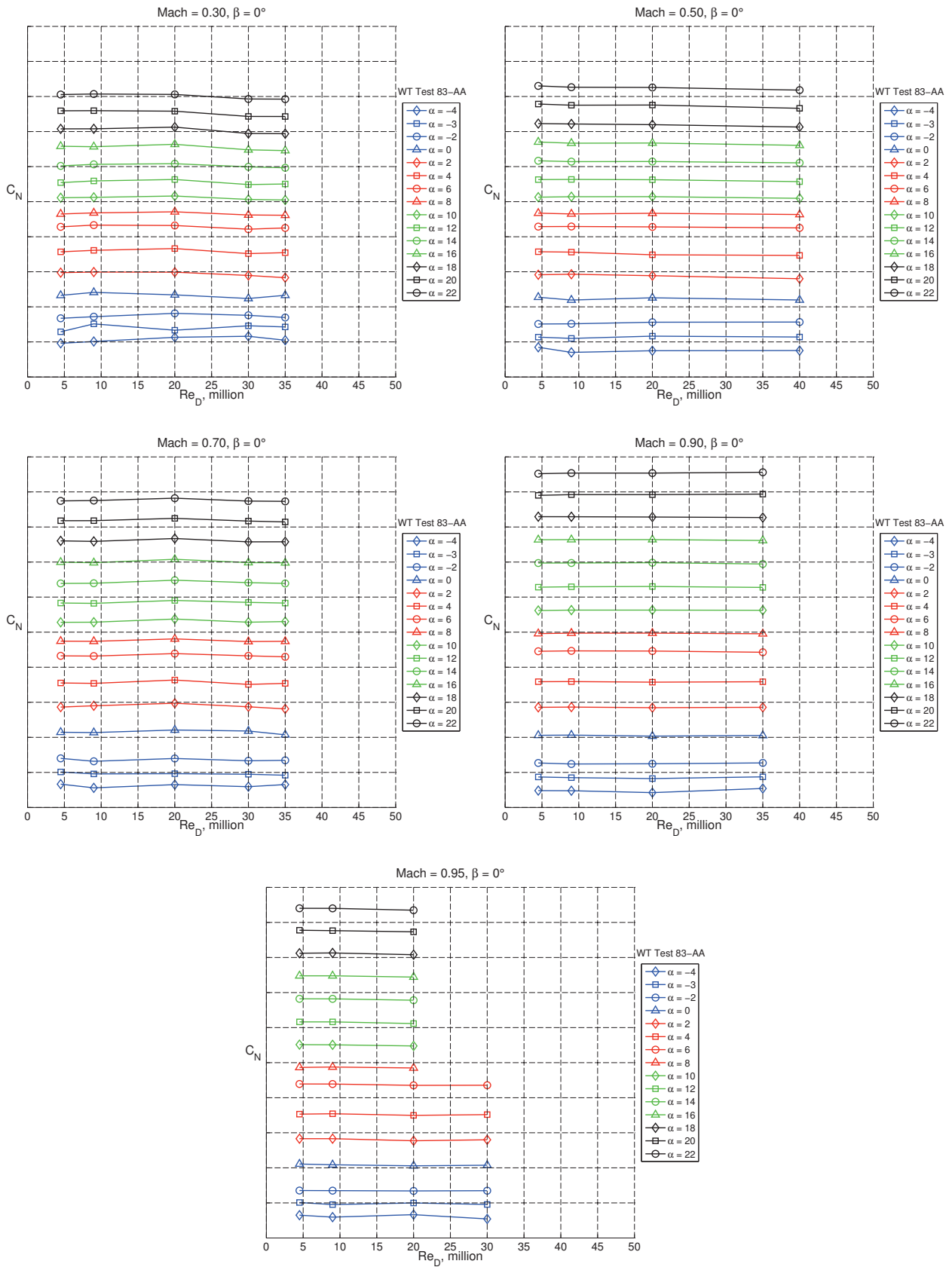
Figure 23. Trend in normal force coefficient with Reynolds number.

American Institute of Aeronautics and Astronautics
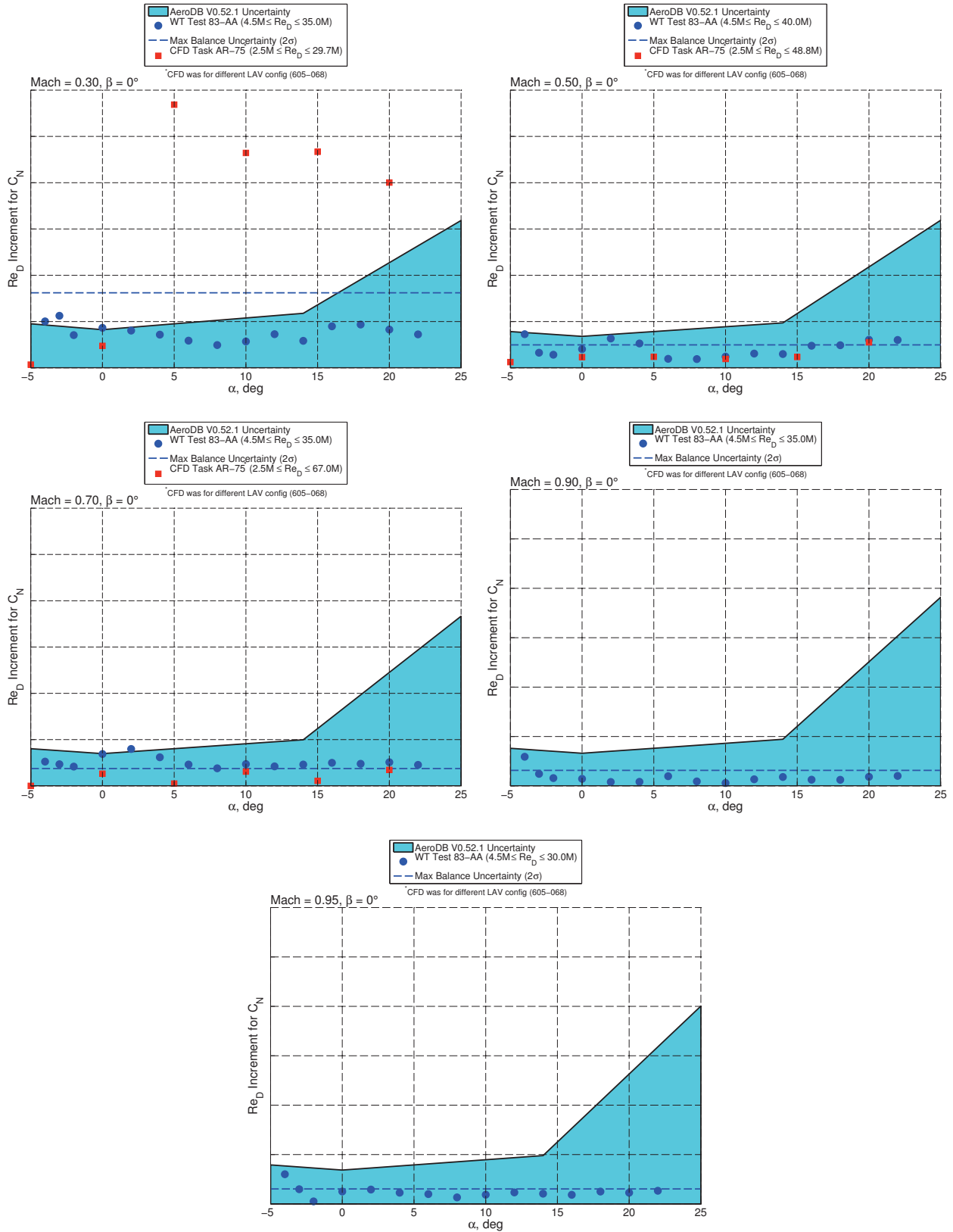
Figure 24. Comparison between wind tunnel data and CFD of the range in normal force coefficient over Reynolds number range.

American Institute of Aeronautics and Astronautics
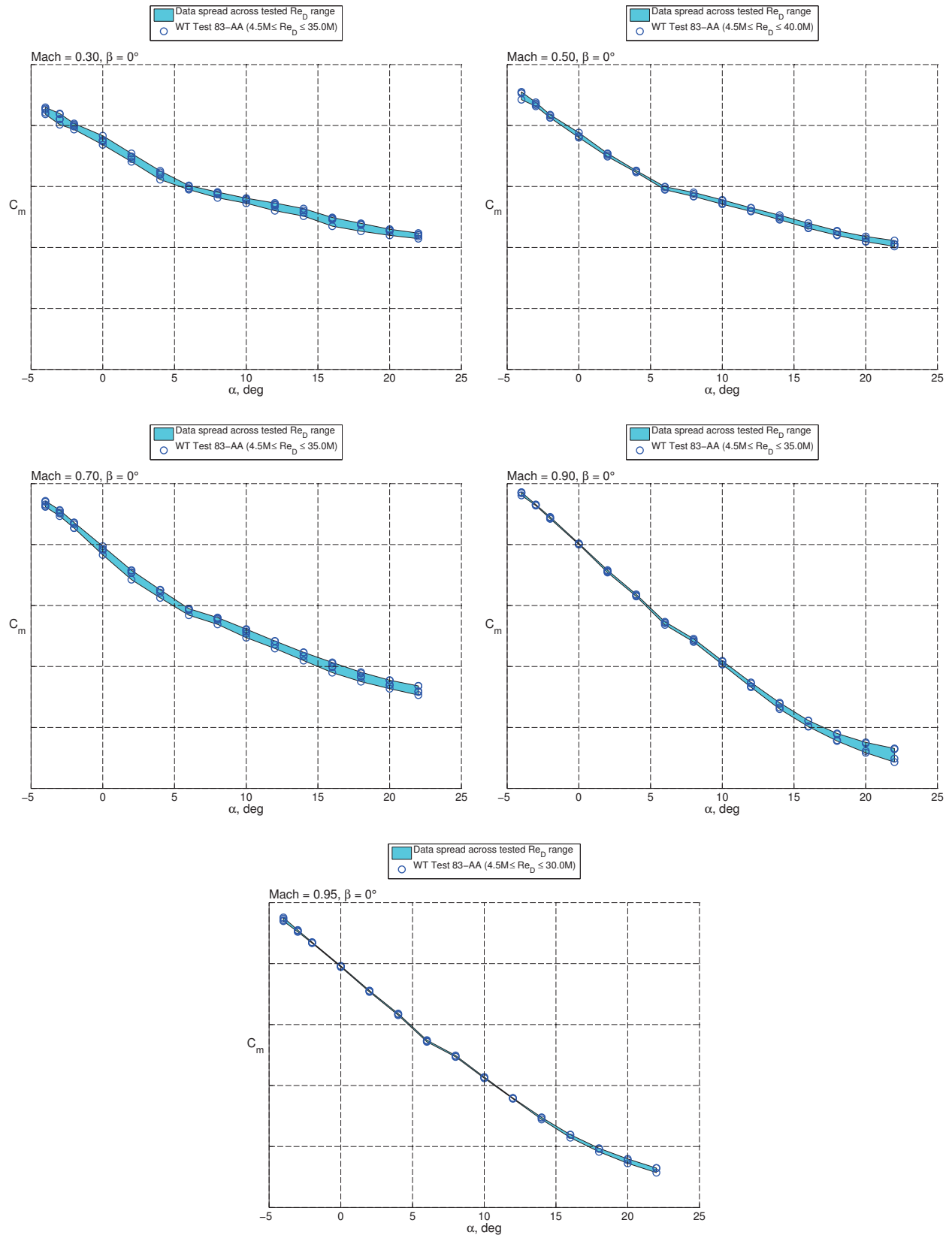
Figure 25. Data spread in pitching moment coefficient across tested Reynolds number range.

American Institute of Aeronautics and Astronautics
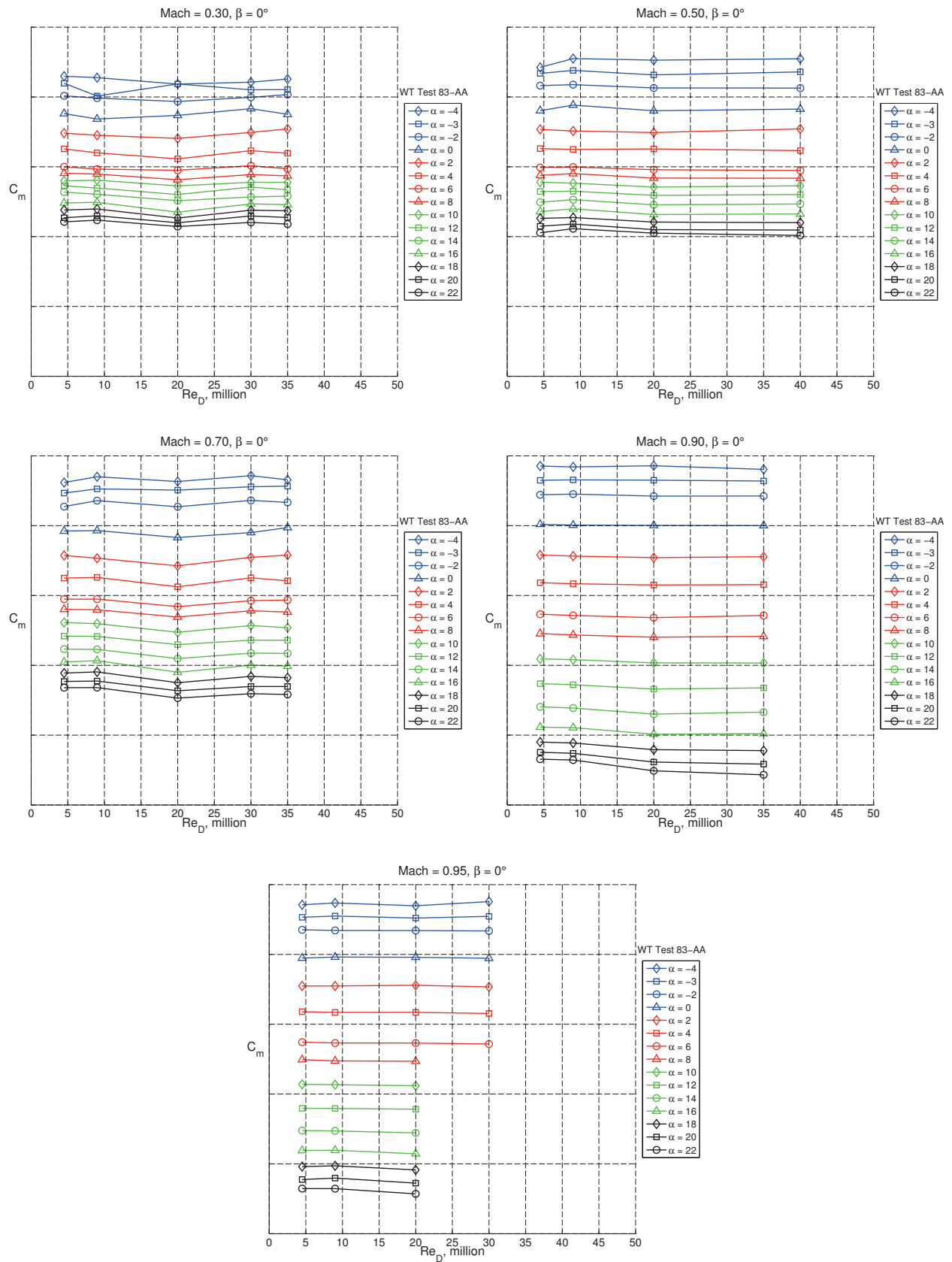
Figure 26. Trend in pitching moment coefficient with Reynolds number.

Figure 27. Comparison between wind tunnel data and CFD of the range in pitching moment coefficient over Reynolds number range.

American Institute of Aeronautics and Astronautics
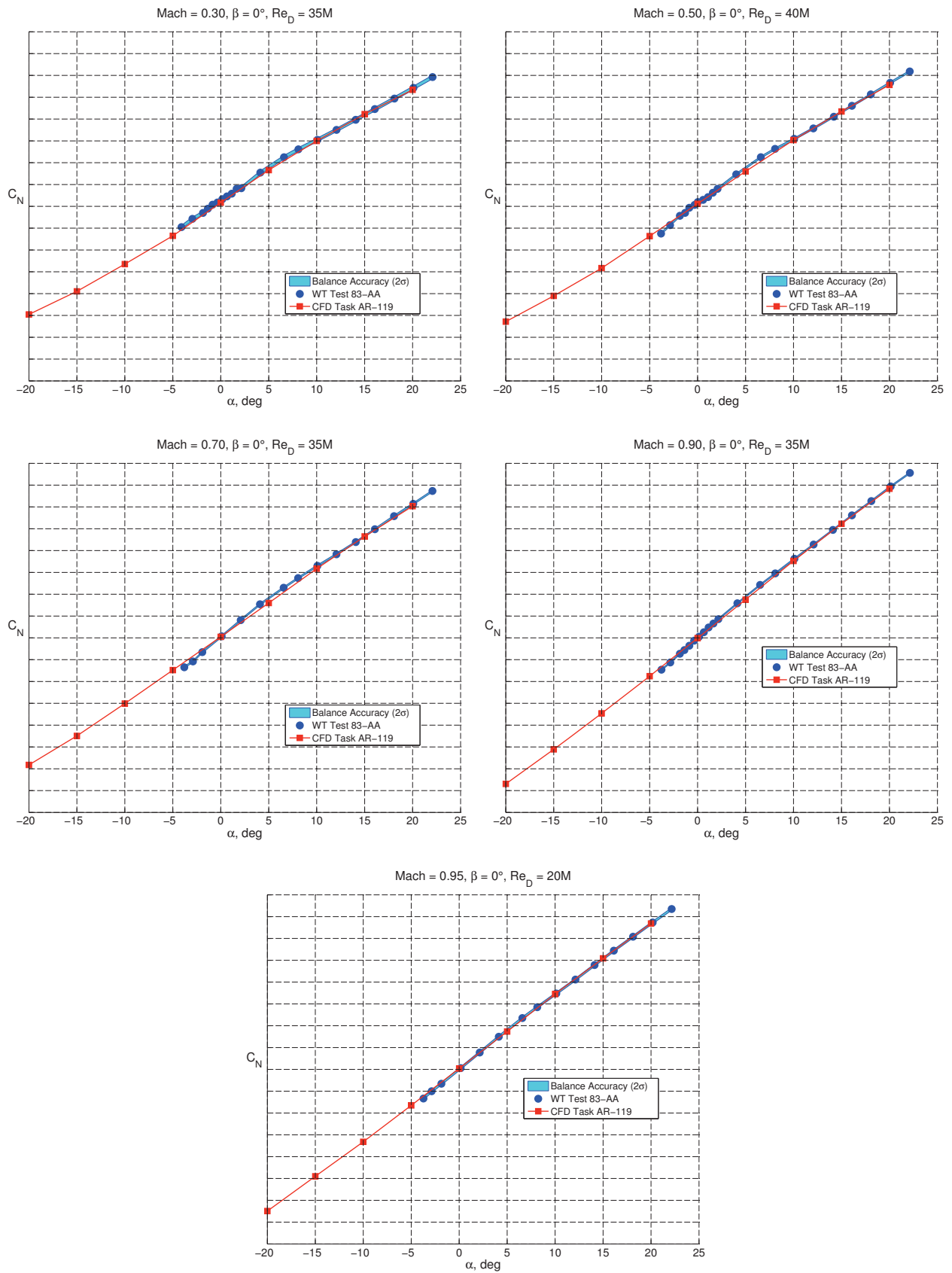
Figure 28. Results of CFD validation exercise for normal force coefficient.
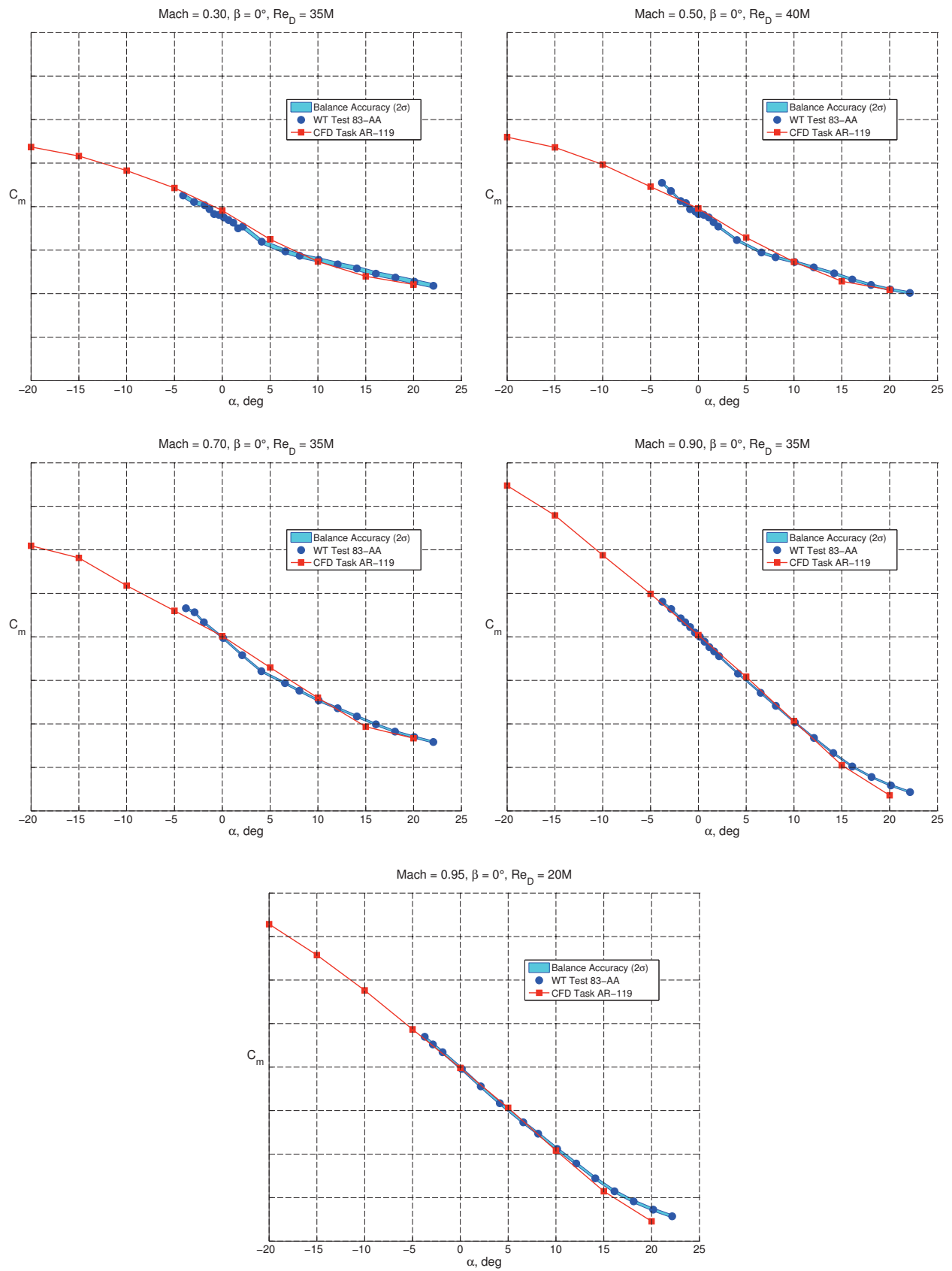
Figure 29. Results of CFD validation exercise for pitching moment coefficient.
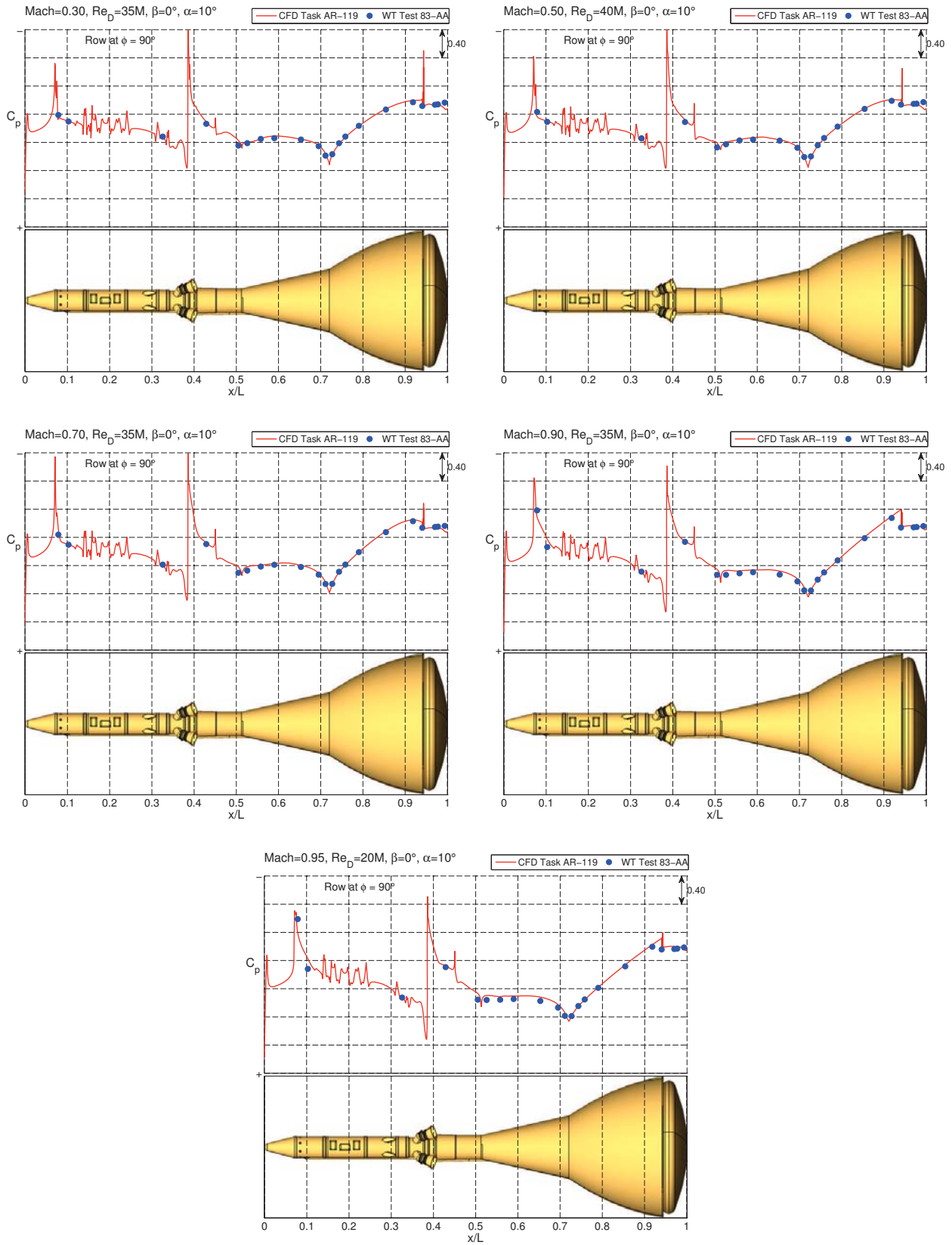
Figure 30. Sample results of CFD validation exercise for static pressures along length of LAV at $\alpha=10°$ for the pressure row at $\phi=90°$.

American Institute of Aeronautics and Astronautics
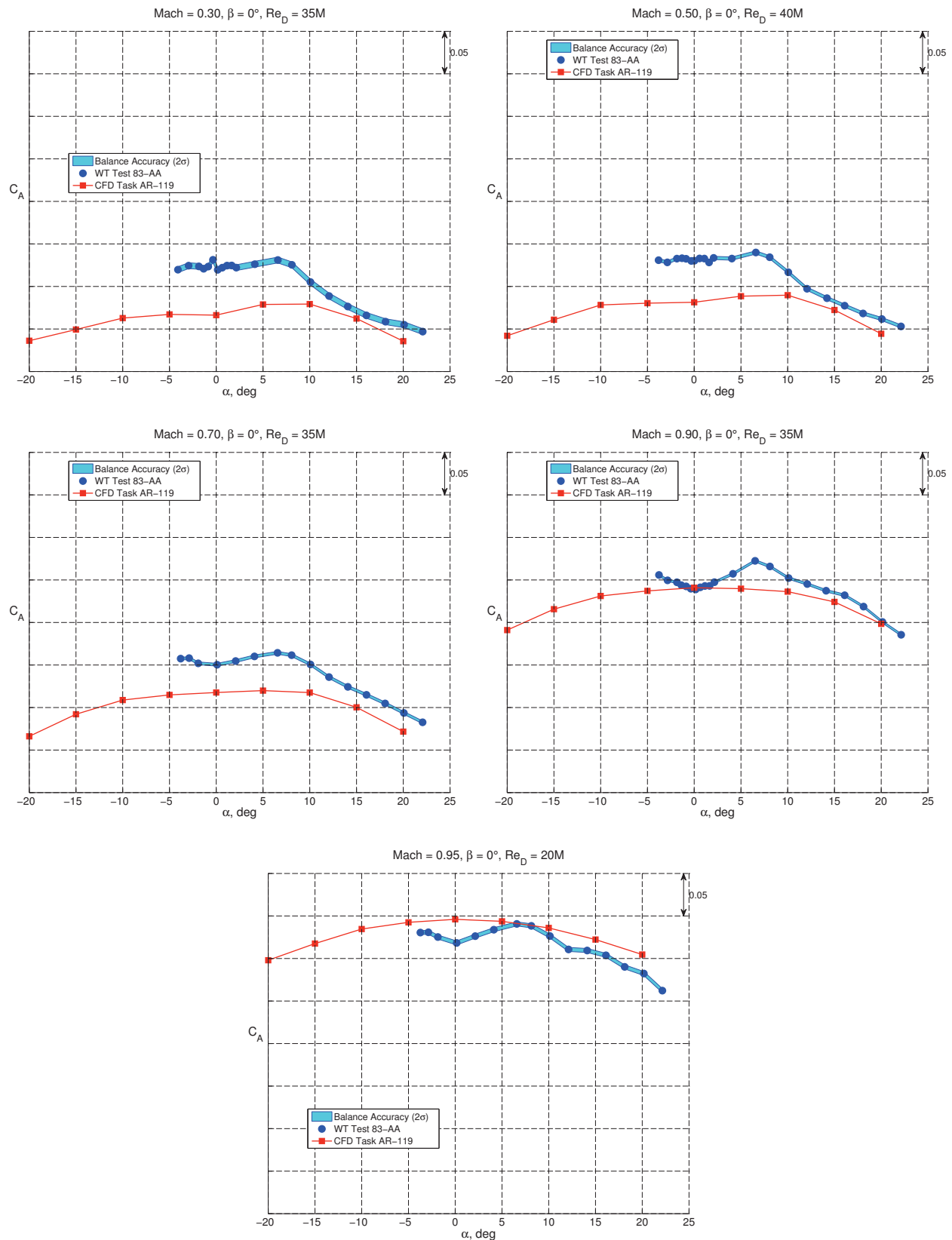
Figure 31. Results of CFD validation exercise for axial force coefficient.
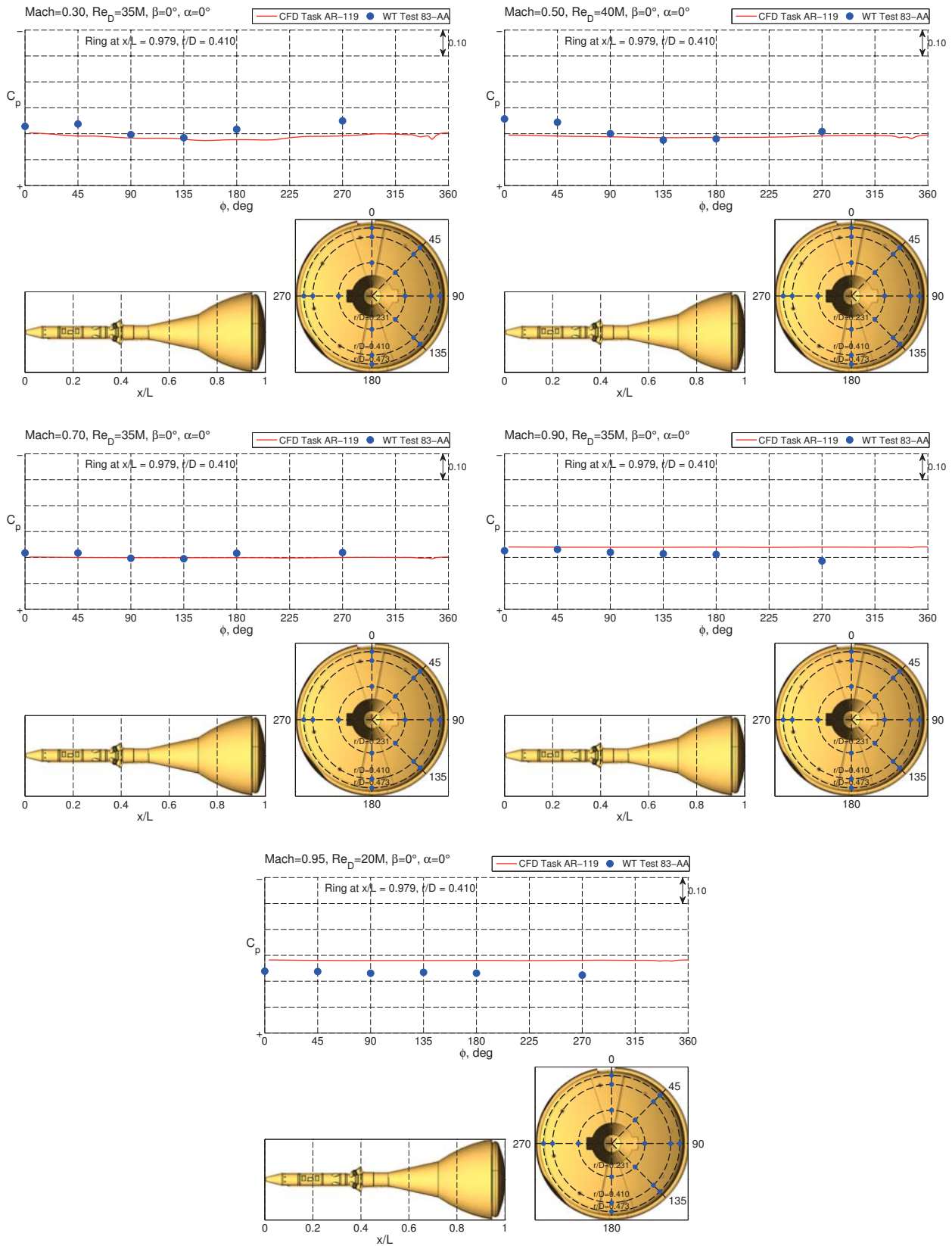
American Institute of Aeronautics and Astronautics
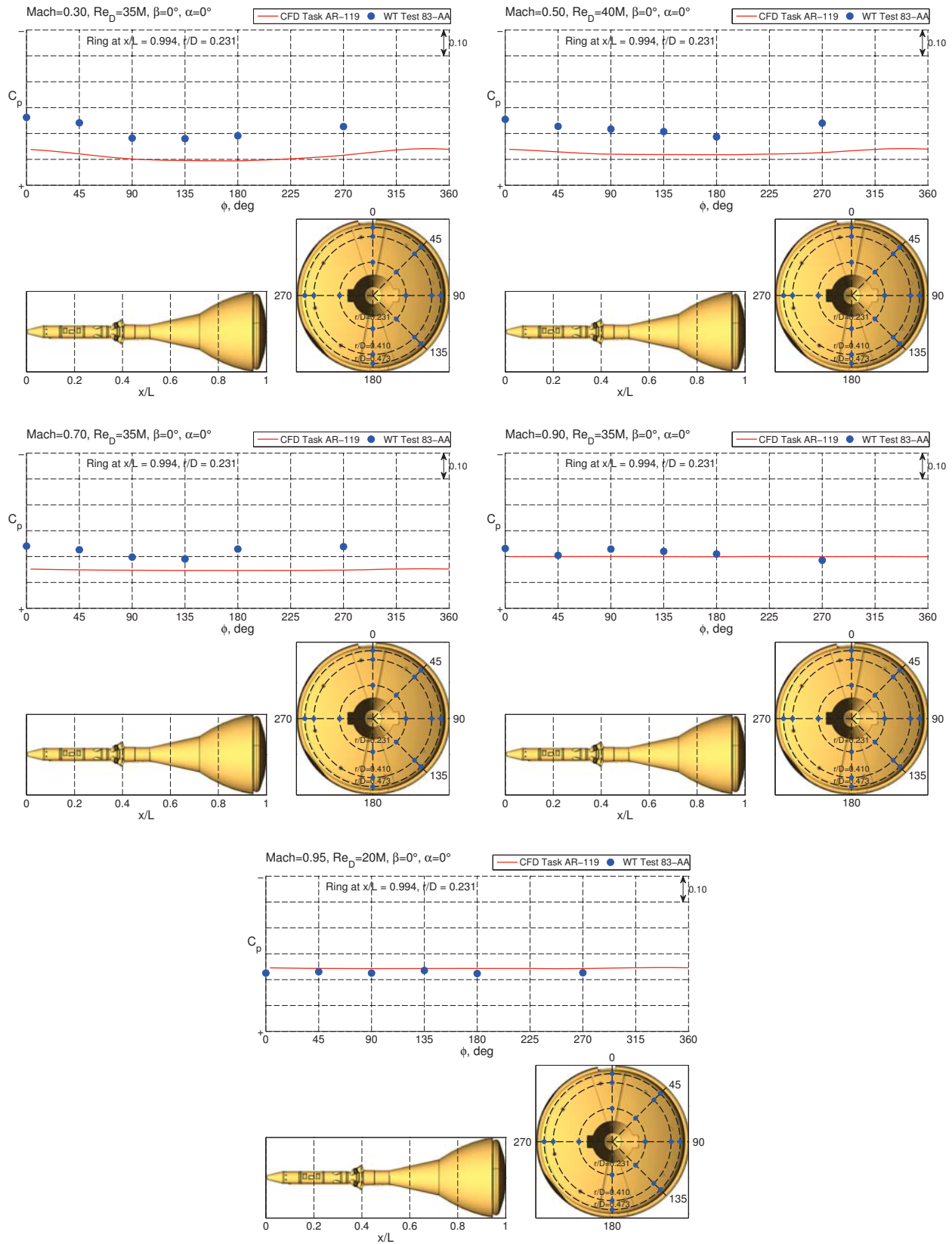
Figure 32. Results of CFD validation exercise for static pressures on inner ring (r/D=0.231) of CM heat shield.

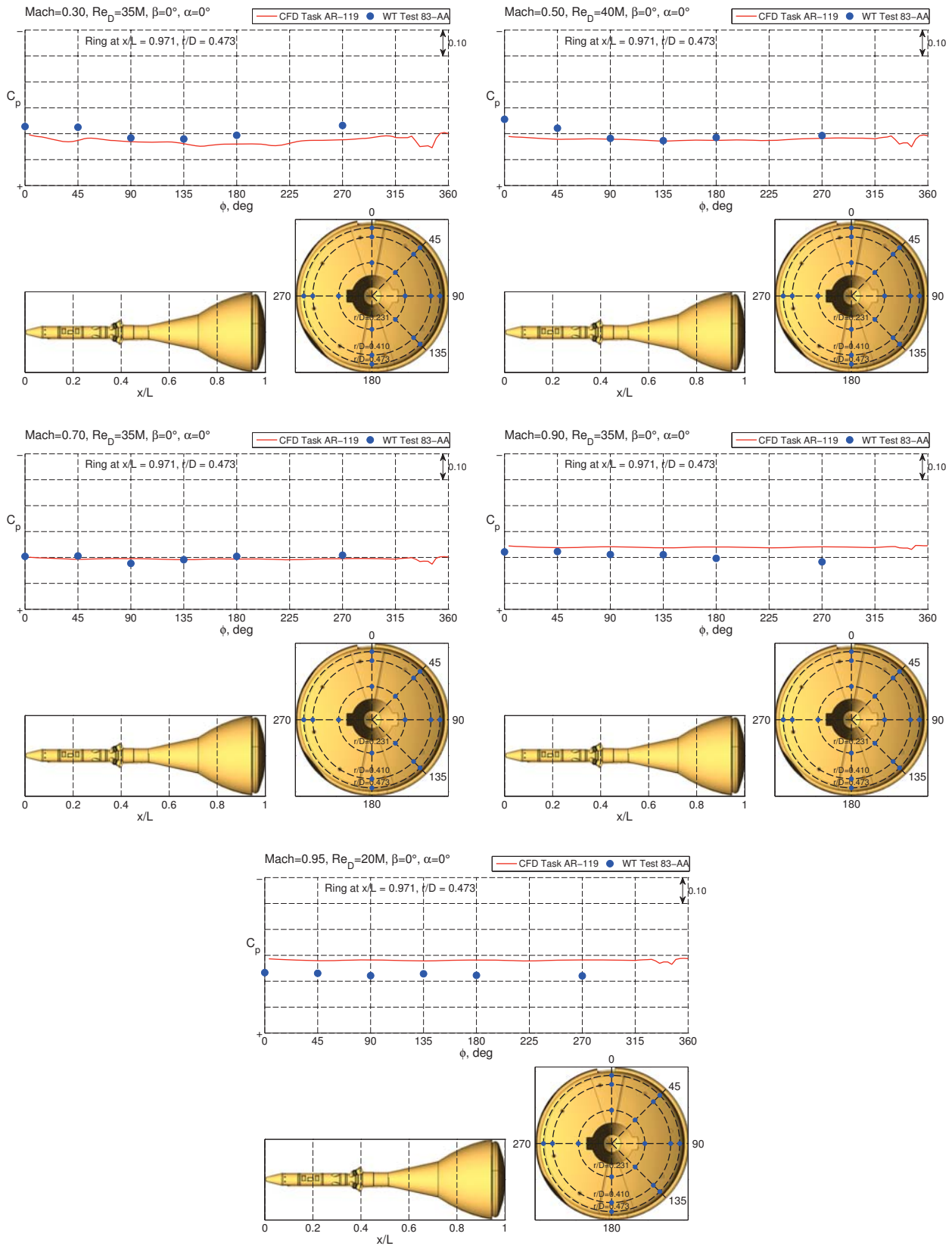Figure 33. Results of CFD validation exercise for static pressures on middle ring (r/D=0.410) of CM heat shield.

Figure 34. Results of CFD validation exercise for static pressures on outer ring (r/D=0.473) of CM heat shield.

American Institute of Aeronautics and Astronautics

(a) WT test 75-AA
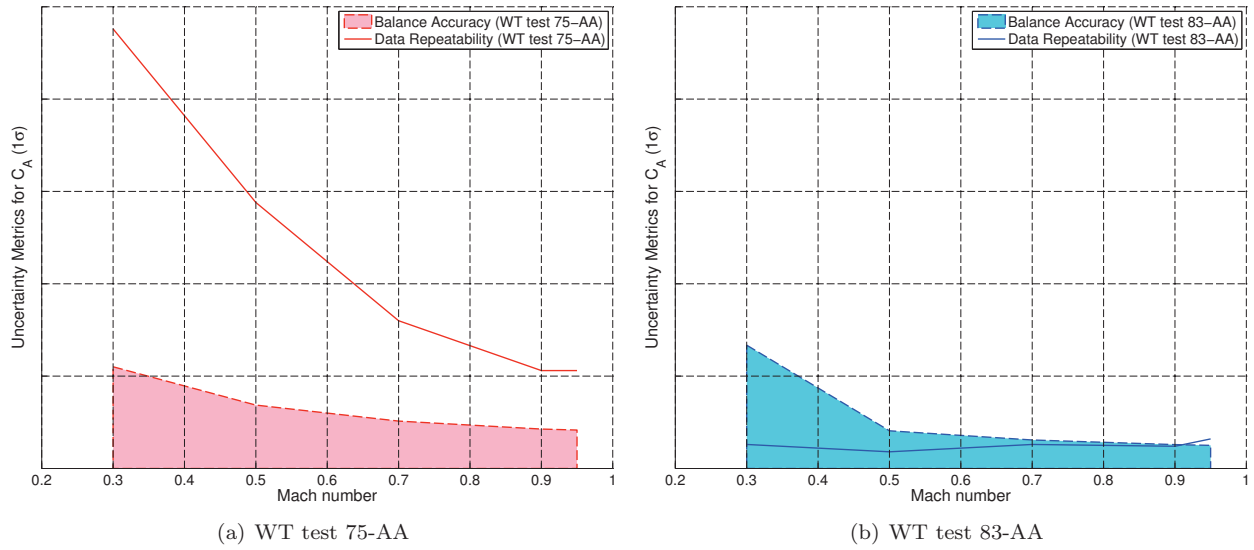
(b) WT test 83-AA

Figure 35. Data repeatability levels for axial force coefficient from two different tests of the unpowered LAV.
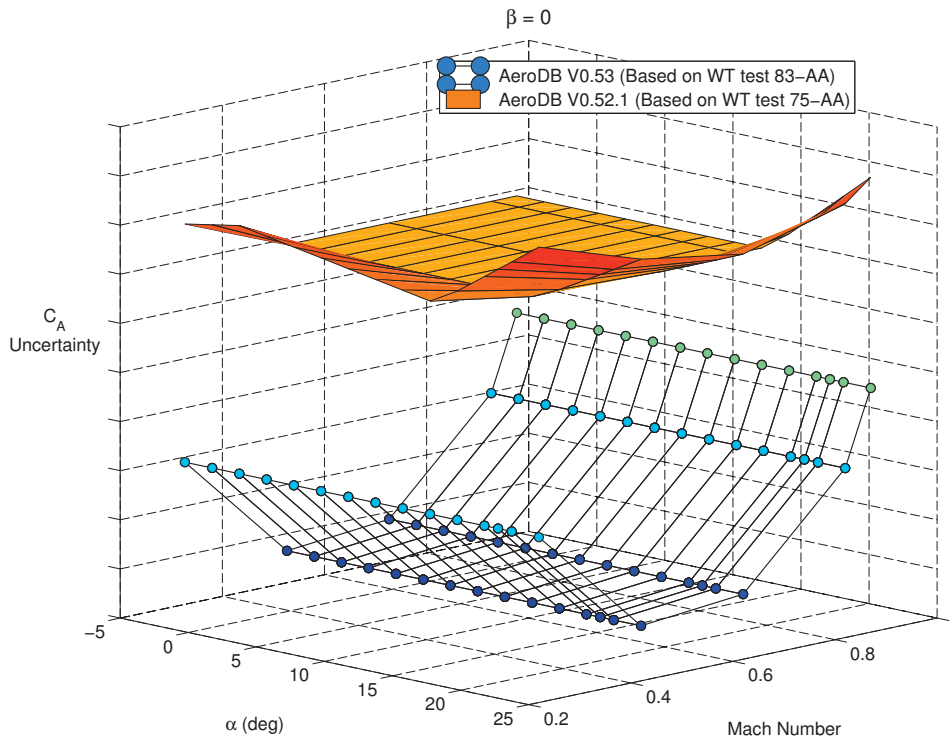

Figure 36. Comparison of database uncertainty of axial force coefficient for the unpowered LAV.

American Institute of Aeronautics and Astronautics